



**HAL**  
open science

## Temperature and Humidity Control of a Micro PEM Fuel Cell Stack

Christian Kunde, Richard Hanke-Rauschenbach, Michael Mangold, Achim Kienle, Kai Sundmacher, Stefan Wagner, Robert Hahn

► **To cite this version:**

Christian Kunde, Richard Hanke-Rauschenbach, Michael Mangold, Achim Kienle, Kai Sundmacher, et al.. Temperature and Humidity Control of a Micro PEM Fuel Cell Stack. Fuel Cells, 2010, 10 (6), pp.949. 10.1002/fuce.201000022 . hal-00574811

**HAL Id: hal-00574811**

**<https://hal.science/hal-00574811>**

Submitted on 9 Mar 2011

**HAL** is a multi-disciplinary open access archive for the deposit and dissemination of scientific research documents, whether they are published or not. The documents may come from teaching and research institutions in France or abroad, or from public or private research centers.

L'archive ouverte pluridisciplinaire **HAL**, est destinée au dépôt et à la diffusion de documents scientifiques de niveau recherche, publiés ou non, émanant des établissements d'enseignement et de recherche français ou étrangers, des laboratoires publics ou privés.



## Temperature and Humidity Control of a Micro PEM Fuel Cell Stack

Journal:	<i>Fuel Cells</i>
Manuscript ID:	face.201000022.R1
Wiley - Manuscript type:	Original Research Paper
Date Submitted by the Author:	13-Apr-2010
Complete List of Authors:	Kunde, Christian; Otto-von-Guericke University, Electrical Engineering Hanke-Rauschenbach, Richard; Max-Planck-Institut Magdeburg mangold, michael; Max-Planck-Institut Magdeburg Kienle, Achim; Otto-von-Guericke University, Electrical Engineering; Max-Planck-Institut Magdeburg Sundmacher, Kai; Max-Planck-Institut Magdeburg Wagner, Stefan; Fraunhofer IZM Berlin, HDI & WLP Hahn, Robert; Fraunhofer IZM Berlin, HDI & WLP
Keywords:	Control, Dynamic Simulation, Portable, Mathematical Model, PEM Fuel Cell System, Water Management



1  
2  
3  
4  
5  
6  
7  
8 We thank the reviewer for his constructive comments. In response to the suggestions,  
9 we modified the manuscript at various points. All modifications are highlighted in  
10 blue in the revised version. In the following, we give replies to the reviewer's  
11 remarks:

- 12  
13 1. *Fig 1a is just for illustration and can be omitted.*  
14 Figure 1a is omitted in the revised version.
  - 15  
16 2. *Explanation to Fig 1b is given subsequent to Fig 2. The sequence of explanations*  
17 *should be adapted.*  
18 In the revision, the explanations to Figure 1 and Figure 2 are given according to  
19 the sequence of the figures.
  - 20  
21 3. *A comparison to steady-state experimental data should be provided.*  
22 A new Figure 4 and the respective explanatory text have been added in the  
23 revision to include steady-state experimental results. Measurements of the high  
24 frequency impedance as a key indicator for the membrane humidification are  
25 given.
  - 26  
27 4. *The transition to a step response are calculated and measured. However no direct*  
28 *comparison is possible due to different setups. I suggest to adjust the parameters*  
29 *of the model to the experimental setup in order to provide a direct comparison.*  
30 The simulation of the step response is now done for parameters adapted to the  
31 experimental setup of Figure 6 and an explanatory text to the differences between  
32 both experimental setups is given. Since the setup according to Figure 6 is  
33 unsuitable for control due to low influence on the stack temperature, the standard  
34 parameters are still used for the rest of the paper.
  - 35  
36 5. *The developed control scheme is simple and developed from analysis of the model*  
37 *behaviour. The effort for an experimental test is relatively low, but no*  
38 *measurements with closed-loop control have been carried out. I suggest to*  
39 *conduct these experiments and to include experimental validation in the*  
40 *publication.*  
41 Actually, our current experimental setup does not yet allow the implementation of  
42 an automatic feedback control. At the moment work on an extended set-up is in  
43 progress, also motivated by the result in this manuscript. However, the design and  
44 manufacturing of a suitable circuit board with a microcontroller and the  
45 programming of the microcontroller will take some time. Our intention is to test  
46 the control scheme as soon as the extension of the experimental setup has been  
47 finished. However, this is beyond the scope of the submitted manuscript. We think  
48 that the proposed control methodology has a value in itself as it is rather general  
49 and maybe applicable to many different fuel cell stacks, not only to the one we  
50 considered in the experiments.
  - 51  
52 6. *Typing error in reference [14].*  
53 Corrected.
- 54  
55  
56  
57  
58  
59  
60

# Temperature and Humidity Control of a Micro PEM Fuel Cell Stack

C. Kunde<sup>a</sup>, R. Hanke-Rauschenbach<sup>a</sup>, M. Mangold<sup>\*,a</sup>, A. Kienle<sup>a,b</sup>,  
K. Sundmacher<sup>a,c</sup>, S. Wagner<sup>d</sup>, R. Hahn<sup>d</sup>

<sup>a</sup> Max-Planck-Institut für Dynamik komplexer technischer Systeme, Sandtorstraße 1, 39106 Magdeburg, Germany

<sup>b</sup> Otto-von-Guericke-Universität Magdeburg, Lehrstuhl für Automatisierungstechnik / Modellbildung, Universitätsplatz 2, 39106 Magdeburg, Germany

<sup>c</sup> Otto-von-Guericke Universität Magdeburg, Lehrstuhl für Systemverfahrenstechnik, Universitätsplatz 2, 39106 Magdeburg, Germany

<sup>d</sup> Fraunhofer Institut für Zuverlässigkeit und Mikrointegration Berlin, Gustav-Meyer-Allee 25, 13355 Berlin, Germany

Received

[\*] Corresponding Author, [mangold@mpi-magdeburg.mpg.de](mailto:mangold@mpi-magdeburg.mpg.de)

## Abstract

This paper deals with the control of a miniaturized fuel cell system. A single air blower is used to control both heat and water management of the fuel cell. As the number of manipulated variables is smaller than the number of control variables, classical control algorithms are not applicable. To find a suitable controller, a system model is developed that shows the qualitatively same behavior as the experimental setup. The dynamic behavior of the model and the influence of the blower are studied by phase portraits. A control algorithm is then conceived by qualitative analysis of the phase portraits and tested in simulations.

**Keywords:** control, miniature fuel cell stack, PEM fuel cell, simulation

## 1 Introduction

Fuel cells directly convert chemical energy to electrical energy. However, they are not well established yet in general applications because of their high costs, limited lifespan and high demands on operation control. With further development fuel cells are expected to play an important part in the future use of renewable energy sources.

Fuel cells have very different fields of application. Depending on the specific application, there are large differences in the mode of operation, the available manipulated variables, the limits for weight, costs and volume of the system and hence in the challenges on process control. In this work the focus is on a miniature fuel cell system for portable applications. This system should be as light, small and cheap as possible. Further, the parasitic power consumption of peripheral devices should be kept small, as it has a much stronger impact on such a low power system than on a high power system. Therefore, the intention is to cut the peripheral equipment to a minimum. Finally, the control algorithm should be implemented on a micro-controller with limited computational power. This prohibits the use of highly ambitious nonlinear control approaches. An uncontrolled open-loop operation of miniature fuel cells is also of limited value, as was shown by Shkolnikov et al. [12]

1  
2  
3  
4  
5  
6  
7  
8 who studied a 2 W power supply without extra humidification, heating or cooling.  
9 Though the system is designed for “free-breathing” operation, they conclude by  
10 experimental results that a blower is needed for optimal operation of their H<sub>2</sub>-  
11 PEMFC. In conclusion, control schemes are needed for micro fuel cell systems with  
12 low system complexity.

13 In open literature, there are hardly suitable solutions to this kind of control  
14 problem. The majority of publications on control of PEMFCs concerns classical  
15 linear control approaches [10, 3, 6, 5, 15], mainly automotive applications. Typically,  
16 a humidifier, a compressor and an independent cooling system are used to control  
17 various system states. Such a control strategy cannot be adapted to miniaturized fuel  
18 cells.

19 There are also some nonlinear approaches for control of PEMFCs [2, 1, 7, 9], but  
20 those are computationally too expensive for micro fuel cell applications.

21 Schumacher et al. [11] propose a fuzzy algorithm for the control of the humidity  
22 in a miniature H<sub>2</sub>-PEMFC. The fuzzy rules use measurements of the impedance and  
23 the voltage of the fuel cell to set the system blower voltage. Test results for an  
24 experimental setup are also shown in that paper. A drawback of their solution is that  
25 they only consider the humidity while the temperature of the fuel cell has still to be  
26 kept constant via additional heating and cooling.

27 In the present study, a control algorithm is proposed that considers both humidity  
28 and temperature of a H<sub>2</sub>-PEMFC system while using only the airflow of a single  
29 blower as a manipulated variable.

30 The following section gives an introduction to the micro fuel cell system. In  
31 section 3 a simplistic model for this fuel cell system is derived and compared with  
32 experimental results. The model is subsequently used in section 4 for controller  
33 design and testing.

## 34 35 2 Micro Fuel Cell Stack

36 In this paper a miniaturized fuel cell system for power output below 20 W is  
37 investigated. The system has been developed by the Fraunhofer IZM Berlin. It has to  
38 be light-weighted and small to fulfill the demands of applications in e.g. portable  
39 electronics, small unmanned vehicles and autonomous sensors. Parasitic power  
40 consumption of peripherals should also be considerably smaller than the total power  
41 output. Any peripherals have to be kept at a minimum for these reasons.

42 Consequently, a single blower is used for the cooling and the air supply of this  
43 fuel cell system. The airflow of this blower is splitted in one fraction that provides the  
44 cathode with oxygen and removes product water vapor from the system. The second  
45 fraction passes over external cooling fins to remove heat from the system. This  
46 concept is shown in Figure 1. The ratio between external and internal airflow is  
47 determined by the geometry of the construction. It influences the general  
48 humidification of the fuel cell and is therefore an important design parameter.

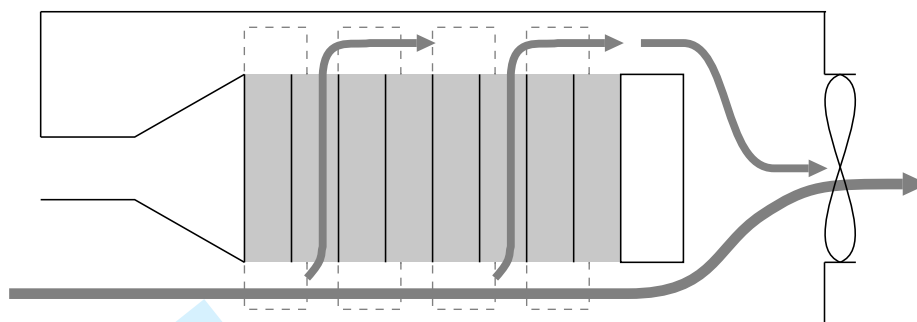
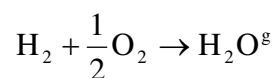


Figure 1: Scheme of the airflow in the fuel cell system. The light grey area in the center represents the fuel cell stack.

H<sub>2</sub>-PEMFCs are used in the investigated system. They can be operated sufficiently well at low temperatures near ambient conditions and involve a less complex chemical reaction than other competitors in the low temperature range. The core of the system is a stack consisting of ten fuel cells connected electrically in series with an active reaction area of 10 cm<sup>2</sup> each.

In the fuel cells, hydrogen is oxidized to water according to the following overall reaction.



The free reaction enthalpy is partly converted to electrical energy. The rest is dissipated and released as heat. The basic configuration of a single fuel cell is illustrated in Figure 2.

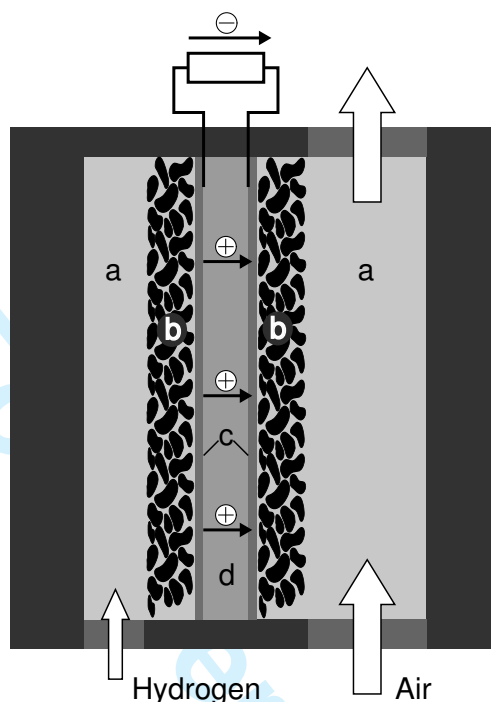


Figure 2: Basic configuration of a H<sub>2</sub>-PEMFC with a) gas channels b) gas diffusion layers c) electrodes and d) the membrane. The anode side is operated in dead-end mode here.

The protonic conductivity of the membrane strongly depends on its humidification. Since humidifiers are not applicable to the system, dry hydrogen is fed to the fuel cell. Additionally, the osmotic drag drives water through the membrane to the cathode side and water is only produced in the cathodic electrode. Therefore humidification of the anode side of the membrane only works by back-diffusion of water from the cathode side to the anode side. To reduce local dehydration, the membrane is chosen as thin as possible.

To further reduce peripherals there is no recirculation of hydrogen. Instead the anodic gas channels are operated in the so called dead-end mode, i. e. the outlet of the anodic gas channels is closed. Since impurities can accumulate in the anodic gas channels due to membrane crossover and impurities in the hydrogen feed, the anodic gas channels have to be purged periodically by briefly opening the anode outlet.

There are several requirements for the operation of the fuel cell system. The membrane has to be kept well humidified for good proton conductivity. The humidity also has to be kept low enough that water does not condensate in the fuel cell, because it would block the gas transport to the reaction sites. The temperature of the fuel must not exceed upper boundaries given by the materials used in the system. The reaction kinetics on the opposite require high temperatures. Additionally, the strong coupling between the temperature and the relative humidity has to be taken into account.

These requirements have to be met by using only the airflow of the blower as a manipulated variable and with a control algorithm that can be easily implemented and run on a microcontroller.

### 3 Derivation of Model Equations

In the following, a control-oriented model for a H<sub>2</sub>-PEMFC is derived, that focuses on heat and water management of the system. The notation used in the subsequent sections is given in Table 1 and Table 2.

#### 3.1 Model Structure and Basic Model Assumptions

The model is a lumped system that describes the dynamics of the fuel cell stack in terms of cell temperature and water vapor concentration in the cathodic gas channels. The following main model assumptions are made:

- Spatial gradients are neglected in the whole system.
- The water content of the membrane is in equilibrium with the cathodic gas channels.
- Local drying of the membrane is not described by the model. The fuel cell performance will therefore be overestimated for higher current densities.
- Water is only present in the membrane and in gaseous form. Liquid water is not accounted for.
- The chemical reaction in the fuel cell produces water in gaseous form.
- The mass storage capacities of the cathodic gas channels and the membrane are dominant. Nitrogen, water vapor and oxygen is present in the cathodic gas channels, the membrane only stores water.
- The heat capacity of the solid parts of the cell is the dominant energy storage capacity.
- The dynamics of the fuel cell are dominated by the water balance and the energy balance. Faster dynamics (e.g. charge balances) are assumed to be instantaneous.
- Voltage losses are caused by the cathodic overvoltage, the protonic resistance of the membrane and the constant ohmic resistance of the electrodes and current collectors. The system is assumed to be connected to an electronic device that sets the output current of the fuel cell stack to specified values.
- The ideal gas law is valid in all gaseous phases.
- The pressure is constant in the whole system.
- Loss of water and heat due to purging of the anodic gas channels is neglected.
- The anodic feed is assumed to be dry, pure hydrogen. The cathodic feed is assumed to be ambient air.

### 3.2 Electrical Model

The computation of a single cell voltage includes the open-circuit voltage  $U_{\text{cell}}^0$  and the voltage loss mechanisms considered in this model, i.e. the cathode activation overpotential, resistance to proton transport in the membrane and resistance to electron transport in the electrodes and the current collectors.

$$U_{\text{cell}} = U_{\text{cell}}^0 + \eta^{\text{C}} - \Delta\phi^{\text{M}} - \Delta\phi^{\Omega} \quad (1)$$

The open circuit voltage is computed using the Nernst equation, where  $\Delta_r G^\theta$  is the standard free reaction enthalpy for the oxidation of hydrogen with the reaction product being water vapor. For the anode side pure hydrogen at approximately standard pressure is assumed. Therefore hydrogen does not appear in the open circuit voltage.

$$U_{\text{cell}}^0 = \frac{-\Delta_r G^\theta}{zF} - \frac{RT_{\text{cell}}}{zF} \cdot \ln\left(\frac{1}{(p_{\text{O}_2} / p)^{1/2}}\right) \quad (2)$$

The relation between current density  $i_{\text{cell}}$  and cathodic overvoltage  $\eta^{\text{C}}$  is described here by the Butler Volmer equation. The exchange current density  $i^{0,\text{C}}$  is dependent on temperature and oxygen concentration. Parameter values for the reaction kinetics are taken from [14].

$$i_{\text{cell}} = -i^{0,\text{C}} \cdot \left( \exp\left(\alpha^{\text{C}} \frac{zF}{RT_{\text{cell}}} \eta^{\text{C}}\right) - \exp\left(-\left(1-\alpha^{\text{C}}\right) \frac{zF}{RT_{\text{cell}}} \eta^{\text{C}}\right) \right) \quad (3)$$

$$i^{0,\text{C}} = i^{0,\text{C,ref}} \cdot \frac{c_{\text{O}_2}^{\text{CC}}}{c_{\text{O}_2}^{\text{ref}}} \cdot \left( \frac{-E_{\text{a}}}{R} \cdot \left( T_{\text{cell}}^{-1} - (T^{\text{ref}})^{-1} \right) \right)$$

The transport of protons through the membrane is driven by the potential difference  $\Delta\phi^{\text{M}}$ . The protonic conductivity  $\kappa_{\text{M}}$  of the membrane depends on the temperature and on the water content of the membrane  $\lambda$ . The according relations are taken from [8].

$$\Delta\phi^{\text{M}} = \frac{i_{\text{cell}}}{\kappa_{\text{M}}} \cdot h_{\text{M}} \quad (4)$$

$$\kappa_{\text{M}} = \kappa_{\text{M},353\text{K}} \cdot \exp\left(-\left(2640 \cdot \exp(-0.6\lambda) + 1183\right) \cdot \left(T_{\text{cell}}^{-1} - (353\text{K})^{-1}\right)\right) \text{K}$$

$$\kappa_{\text{M},353\text{K}} = \left(0.0013\lambda^3 + 0.0298\lambda^2 + 0.2658\lambda\right) \text{S m}^{-1}$$

The ohmic resistances of the electrodes and the current collectors are comprised in the cell resistance  $R_{\text{cell}}$ .

$$\Delta\phi^{\Omega} = i_{\text{cell}} \cdot A_{\text{cell}} \cdot R_{\text{cell}} \quad (5)$$

### 3.3 Mass Balances

First the **oxygen balance** should be derived. The dynamics of the oxygen concentration in the cathodic gas channels is assumed to be fast in comparison with the water dynamics and the temperature dynamics. The quasi-stationary material balance reads:

$$0 = x_{\text{O}_2}^{\text{in}} F^{\text{in,CC}} - \frac{c_{\text{O}_2}^{\text{CC}}}{p^{\text{CC}} / RT_{\text{cell}}} F^{\text{out}} - \frac{1}{2} \frac{nA_{\text{cell}} i_{\text{cell}}}{zF} \quad (6)$$

The equation given above can be converted into an explicit expression for the oxygen concentration in the cathode channels  $c_{\text{O}_2}^{\text{CC}}$ . The unknown cathodic molar outflow  $F^{\text{out}}$  will be looked at the end of this subsection.

Next the **water balance** is developed. An approach according to [4] is followed here. The integral water balance around the whole stack reads:

$$\frac{dn_{\text{H}_2\text{O}}}{dt} = x_{\text{H}_2\text{O}}^{\text{in}} F^{\text{in,CC}} - x_{\text{H}_2\text{O}}^{\text{CC}} F^{\text{out}} + \frac{nA_{\text{cell}} i_{\text{cell}}}{zF} \quad (7)$$

In the balance given above the anodic inflow does not appear as the hydrogen feed enters the cell dry.

The water is assumed to distribute homogeneously in the membrane and the cathode gas compartment. Due to its small volume the anodic gas compartment was neglected.

$$n_{\text{H}_2\text{O}} = V^{\text{CC}} c_{\text{H}_2\text{O}}^{\text{CC}} + V^{\text{M}} c_{\text{H}_2\text{O}}^{\text{M}} \quad (8)$$

As mentioned before the cathodic gas compartment and the membrane are assumed to be in thermodynamic equilibrium. The membrane water concentration can therefore be expressed as a function of the channel water concentration and the temperature.

$$c_{\text{H}_2\text{O}}^{\text{M}} = c_{\text{H}_2\text{O}}^{\text{M}}(c_{\text{H}_2\text{O}}^{\text{CC}}, T_{\text{cell}}) \quad (9)$$

The expression given above is established by the following set of constitutive equations [8], forming the algebraic sub-system (10)–(16).

$$c_{\text{H}_2\text{O}}^{\text{M}} = \lambda X \rho_{\text{M}} \quad (10)$$

with

$$X = \frac{X^{\text{dry}}}{1 + \lambda X \rho_M} \quad (11)$$

$$\rho_M = \rho_{\text{H}_2\text{O}} \rho_M^{\text{dry}} \frac{1 + \lambda M_{\text{H}_2\text{O}} X^{\text{dry}}}{\rho_{\text{H}_2\text{O}} + \rho_M^{\text{dry}} \lambda M_{\text{H}_2\text{O}} X^{\text{dry}}} \quad (12)$$

The water phase equilibrium relation reads

$$\lambda(T_{\text{cell}}) = \lambda_{303\text{K}} + \frac{T_{\text{cell}} - 303\text{K}}{50\text{K}} \cdot (\lambda_{353\text{K}} - \lambda_{303\text{K}}) \quad (13)$$

$$\lambda_{303\text{K}} = 0.043 + 17.81a_{\text{H}_2\text{O}} - 39.85a_{\text{H}_2\text{O}}^2 + 36a_{\text{H}_2\text{O}}^3 \quad (14)$$

$$\lambda_{353\text{K}} = 0.3 + 10.8a_{\text{H}_2\text{O}} - 16a_{\text{H}_2\text{O}}^2 + 14.1a_{\text{H}_2\text{O}}^3 \quad (15)$$

with the water activity  $a_{\text{H}_2\text{O}}$  or the channel relative humidity  $rH$  defined as

$$a_{\text{H}_2\text{O}} = rH = \frac{c_{\text{H}_2\text{O}}^{\text{CC}} RT_{\text{cell}}}{p_{\text{sat}}(T_{\text{cell}})} \quad (16)$$

For numerical treatment and the subsequent controller synthesis it is convenient to express the water balance (7) in terms of  $dn_{\text{H}_2\text{O}}/dt$ . Time derivation of Equations (8) and (9) gives

$$\frac{dn_{\text{H}_2\text{O}}}{dt} = V^{\text{CC}} \cdot \frac{dc_{\text{H}_2\text{O}}^{\text{CC}}}{dt} + V^{\text{M}} \frac{\partial c_{\text{H}_2\text{O}}^{\text{M}}}{\partial c_{\text{H}_2\text{O}}^{\text{CC}}} \cdot \frac{dc_{\text{H}_2\text{O}}^{\text{CC}}}{dt} + V^{\text{M}} \frac{\partial c_{\text{H}_2\text{O}}^{\text{M}}}{\partial T_{\text{cell}}} \cdot \frac{dT_{\text{cell}}}{dt} \quad (17)$$

Substitution of  $dn_{\text{H}_2\text{O}}/dt$  in Equation (7) by the expression given above yields

$$\begin{aligned} & \left( V^{\text{CC}} + V^{\text{M}} \frac{\partial c_{\text{H}_2\text{O}}^{\text{M}}}{\partial c_{\text{H}_2\text{O}}^{\text{CC}}} \right) \cdot \frac{dc_{\text{H}_2\text{O}}^{\text{CC}}}{dt} + V^{\text{M}} \frac{\partial c_{\text{H}_2\text{O}}^{\text{M}}}{\partial T_{\text{cell}}} \cdot \frac{dT_{\text{cell}}}{dt} \\ & = x_{\text{H}_2\text{O}}^{\text{in}} F^{\text{in,CC}} - x_{\text{H}_2\text{O}}^{\text{CC}} F^{\text{out}} + \frac{nA_{\text{cell}} i_{\text{cell}}}{zF} \end{aligned} \quad (18)$$

Finally, a relation for the cathodic molar outflow  $F^{\text{out}}$  should be derived. Starting point is the total material balance for the cathode channel.

$$V^{CC} \frac{dc_t^{CC}}{dt} = F^{in,CC} - F^{out} + \frac{1}{2} \frac{nA_{cell} i_{cell}}{zF} - V^M \frac{dc_{H_2O}^M}{dt} \quad (19)$$

The last term in the equation given above considers the amount of water to be exchanged with the membrane instantaneously in order to obey the thermodynamic equilibrium (9). Time derivation of Equation (9) and multiplication with  $V^M$  gives:

$$V^M \frac{dc_{H_2O}^M}{dt} = V^M \frac{\partial c_{H_2O}^M}{\partial c_{H_2O}^{CC}} \cdot \frac{dc_{H_2O}^{CC}}{dt} + V^M \frac{\partial c_{H_2O}^M}{\partial T_{cell}} \cdot \frac{dT_{cell}}{dt} \quad (20)$$

Using the ideal gas law and considering the assumption of constant pressure Equation (19) can be finally converted to

$$\begin{aligned} F^{out} = F^{in,CC} + \frac{1}{2} \frac{nA_{cell} i_{cell}}{zF} - V^M \frac{\partial c_{H_2O}^M}{\partial c_{H_2O}^{CC}} \cdot \frac{dc_{H_2O}^{CC}}{dt} \\ - V^M \frac{\partial c_{H_2O}^M}{\partial T_{cell}} \cdot \frac{dT_{cell}}{dt} + V^{CC} \frac{p^{CC}}{RT_{cel}^2} \cdot \frac{dT_{cell}}{dt} \end{aligned} \quad (21)$$

### 3.4 Energy Balance

The energy balance for the system reads with  $\dot{H}$  being enthalpy flows and  $P_{el}$  and  $Q_{th}$  being the electrical power and the heat flow drawn from the system:

$$\frac{dE}{dt} = \dot{H}^{in} - \dot{H}^{out} - P_{el} - Q_{th} \quad (22)$$

By incorporating the model assumptions and assuming temperature independent heat capacities the energy balance can be transformed as follows:

$$C_{p,solid} \frac{dT_{cell}}{dt} = F^{in} c_{p,gas} \cdot (T^{amb} - T_{cell}) + \frac{nA_{cell} i_{cell}}{zF} \cdot (-\Delta_r H) - P_{el} - Q_{th}$$

The heat flow  $Q_{th}$  leaving the stack is modelled to be linearly dependent on the temperature difference between fuel cell and environment.

$$Q_{th} = k_{env} \cdot (T_{cell} - T^{amb}) \quad (23)$$

The heat produced by the reaction (second term on right-hand side) can be rewritten using the heating value voltage  $U_{th}$  :

$$U_{th} = \frac{-\Delta_r H}{zF} \quad (24)$$

Using those relations and substituting the electrical power in the energy balance gives the following compact dynamical equation for the cell temperature:

$$C_{p,solid} \frac{dT_{cell}}{dt} = (T^{amb} - T_{cell}) \cdot (F^{in} c_{p,gas} + k_{env}) + nA_{cell} i_{cell} \cdot (U_{th} - U_{cell}) \quad (25)$$

Equation (25) is used in the model, where  $F^{in}$  is the total molar flow entering the system.

$$F^{in} = F^{in,CC} + \frac{nA_{cell} i_{cell}}{zF} \quad (26)$$

The heat transport coefficient  $k_{env}$  is dependent on  $F^{ext}$  and fitted to experimental data.

$$k_{env} = \left(0.078 \text{ mol s}^{-1} \cdot (F^{ext})^{-1} + 0.301\right)^{-1} \text{ W K}^{-1} + 0.05 \text{ W K}^{-1} \quad (27)$$

Additionally, the heat capacity of the gas  $c_{p,gas}$  does not vary much with composition and is assumed to be constant.

### 3.5 Resulting Fuel Cell Model

The resulting fuel cell model consists of two differential equations, the equation for the water content (18) and the equation for the cell temperature (25). For the design of the controller, these equations have to be linked to the power of the air blower that will be used as the manipulated variable. To do this, it is assumed that the external airflow  $F^{ext}$  generated by the blower is equal to the gas flow at the cathode inlet  $F^{in,CC}$  times a constant factor.

$$F^{ext} = 25 \cdot F^{in,CC}$$

Further, an algebraic correlation between  $F^{ext}$  and  $P_{blower}$  is postulated.

$$F^{ext} = F^{ext}(P_{blower})$$

To simplify this study, it is assumed that  $F^{ext}$  can be set directly by the controller.

1  
2  
3  
4  
5  
6  
7  
8 The model is simulated in MATLAB using the parameters given in Table 3.  
9

### 10 **3.6 Simulation and Comparison to Experimental Data**

11 The stationary solutions for a range of the current density are shown in Figure 3.  
12 The other parameters are kept constant. Both the water vapor concentration in the  
13 cathode channels and the cell temperature rise roughly linear with the current density.  
14 This leads to a single maximum for the relative humidity in the channels (Figure 3d).  
15 Depending on the parameters this maximum may be significantly higher than the  
16 environmental humidity. Only a well humidified membrane has a good conductivity  
17 for protons. The effect of self-humidification is therefore necessary for operation of  
18 the system without additional humidification of the inlet gas streams.

19 A similar behavior of the humidity can be observed when the airflow is varied at a  
20 constant cell current (not shown here). Temperature and water concentration increase  
21 approximately linearly with an increase of the reciprocal of  $F^{\text{in,CC}}$ . Again, this leads  
22 to a single maximum in the steady state humidity as a function of  $F^{\text{in,CC}}$ .  
23

24 To validate the stationary behaviour of the model, impedance measurements were  
25 taken at a voltage frequency of 1 kHz. At such a rather high frequency the fuel cell's  
26 impedance can be seen as a measure for its ohmic resistance and hence for the  
27 humidification of the membrane. Figure 4 shows a comparison between the simulated  
28 ohmic resistance and the measured impedance. The qualitative agreement is good.  
29 Both curves show a distinct minimum that is due to a maximum of humidity as  
30 described above. The absolute values of simulated resistance and measured  
31 impedance deviate, because the simulated value includes the membrane resistance  
32 only, whereas the measured impedance additionally contains other ohmic resistances  
33 that are independent of the current density. Further, there is a slight offset between the  
34 simulated and the measured minimum of the impedance. This can be attributed to  
35 unmodelled loss mechanisms such as local drying of the membrane due to osmotic  
36 drag. These losses lead to an increased heat production and therefore a lower  
37 humidification of the membrane than the model would predict.  
38  
39  
40  
41  
42  
43  
44  
45  
46  
47  
48  
49  
50  
51  
52  
53  
54  
55  
56  
57  
58  
59  
60

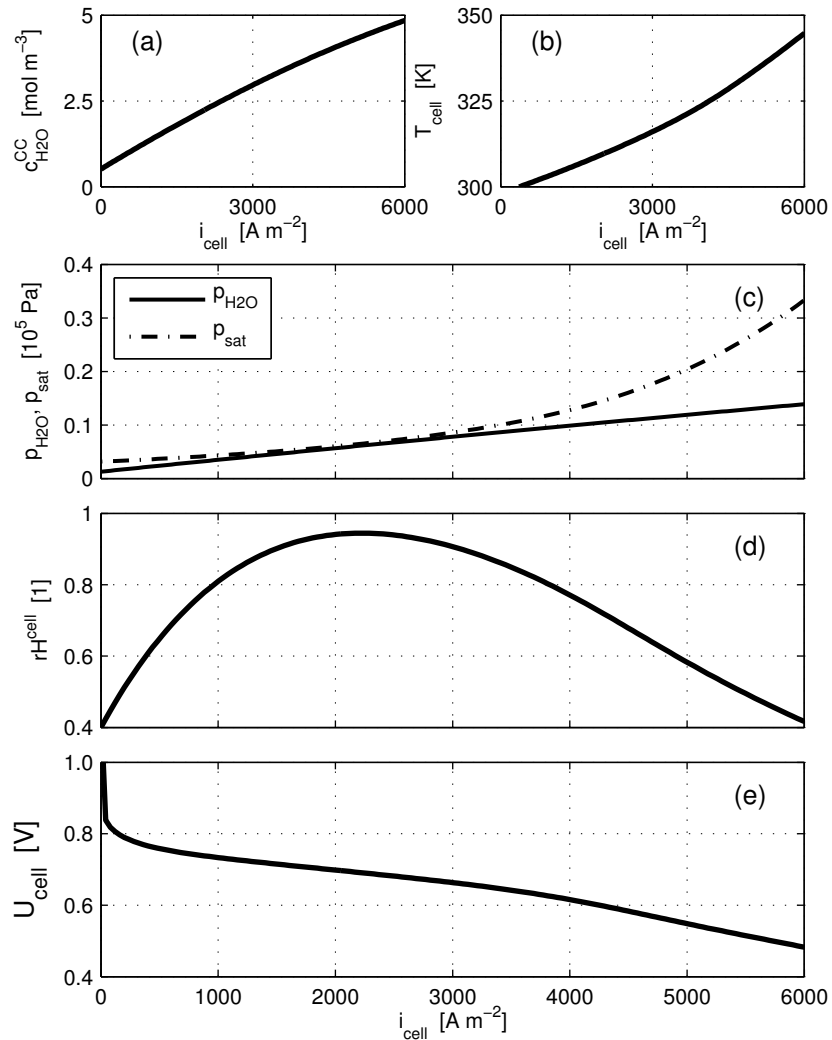


Figure 3: Stationary solutions for the variation of the current density. The airflow is kept constant at  $F^{\text{in,CC}} = 0.0023 \text{ mol s}^{-1}$ . (a) water vapor concentration (b) temperature (c) partial pressure and saturation pressure of water vapor (d) relative humidity (e) cell voltage.

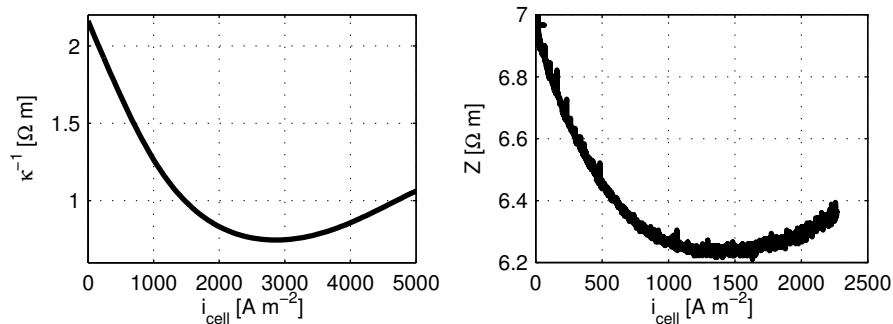


Figure 4: Stationary impedance values for varied current densities. (left) simulation, membrane impedance only, (right) measurement of the whole system. Measurement setup as described in [13]. The airflow is kept constant. The minimum impedance corresponds to a maximum of humidification as shown in Figure 3d.

The validation of the dynamic behavior of the model was done based on a preliminary fuel cell stack design that differs slightly from the final design used for the control studies. The reason is that the preliminary stack design allowed humidity measurements in the stack, which are much harder in the final layout. The preliminary stack differs from the final design in the following points relevant for the model: six instead of ten fuel cells in the stack; no active external cooling, i.e. the heat transfer coefficient  $k_{\text{env}}$  is constant; higher total heat capacity  $C_{\text{p,solid}}$ , because much heavier endplates are used. Therefore the three model parameters  $n$ ,  $k_{\text{env}}$ ,  $C_{\text{p,solid}}$  had to be adapted for comparison with experiments, as indicated in Table 3.

The transient behavior of the fuel cell model shown in Figure 5 reflects the different time constants for the dynamics of temperature and water vapor concentration. Steps of the current density were applied to the system while keeping the other parameters constant (Figure 5a). Changes of the temperature are found to be slower than those of the water vapor concentration. This results in an overshoot of the relative humidity (Figure 5d), because the saturation pressure also changes more slowly than the partial pressure of water vapor. On the rising slope of the relative humidity water is bound by the membrane and partially released on the falling slope. As a consequence there is also an overshoot of the water vapor concentration. Its maximum is shifted towards the falling slope of the relative humidity.

After a step to a higher current density the cell voltage drops instantaneously according to the actual ohmic resistance of the cell. The voltage then reaches temporarily higher values due to better humidification and lower membrane resistance. The maximum of the cell voltage therefore correlates with the maximum of the relative humidity.

A comparison with the experimental results in Figure 6 indicates a reasonable accuracy of the model. One difference is that the simulated temperature approximately follows a linear first-order step response, whereas the measured temperature rises very slowly in the immediate vicinity of the steady-state (Figure 6b). This may be explained by the slow heating of the endplates, which affect the measured temperature in the middle of the stack. To include this effect in the model, the assumption of a homogeneous stack temperature would have to be dropped.

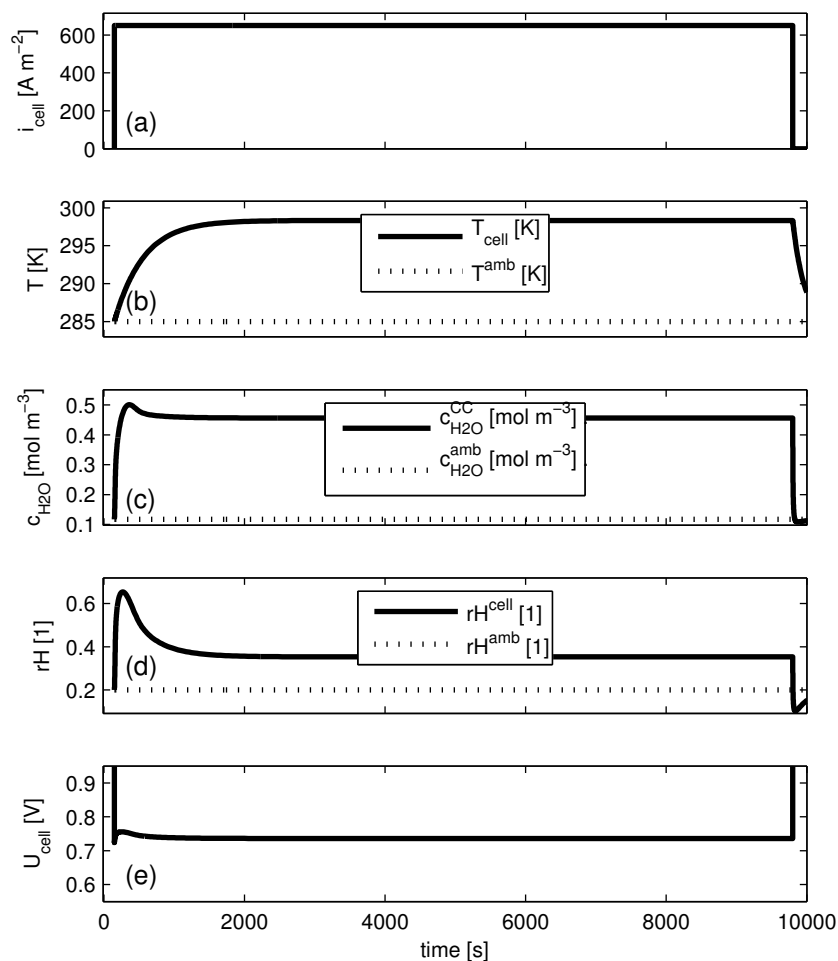


Figure 5: System response to a current density step. The airflow is kept constant at  $F^{\text{in,CC}} = 0.0024 \text{ mol s}^{-1}$ ; (a) current density (b) cell voltage (c) temperature (d) relative humidity (e) water vapor concentration. The overshoot of the relative humidity is due to slower dynamics of the temperature compared to the water vapor concentration. On the falling slope of the humidity water is released from the membrane. This also leads to an overshoot of the water vapor concentration.

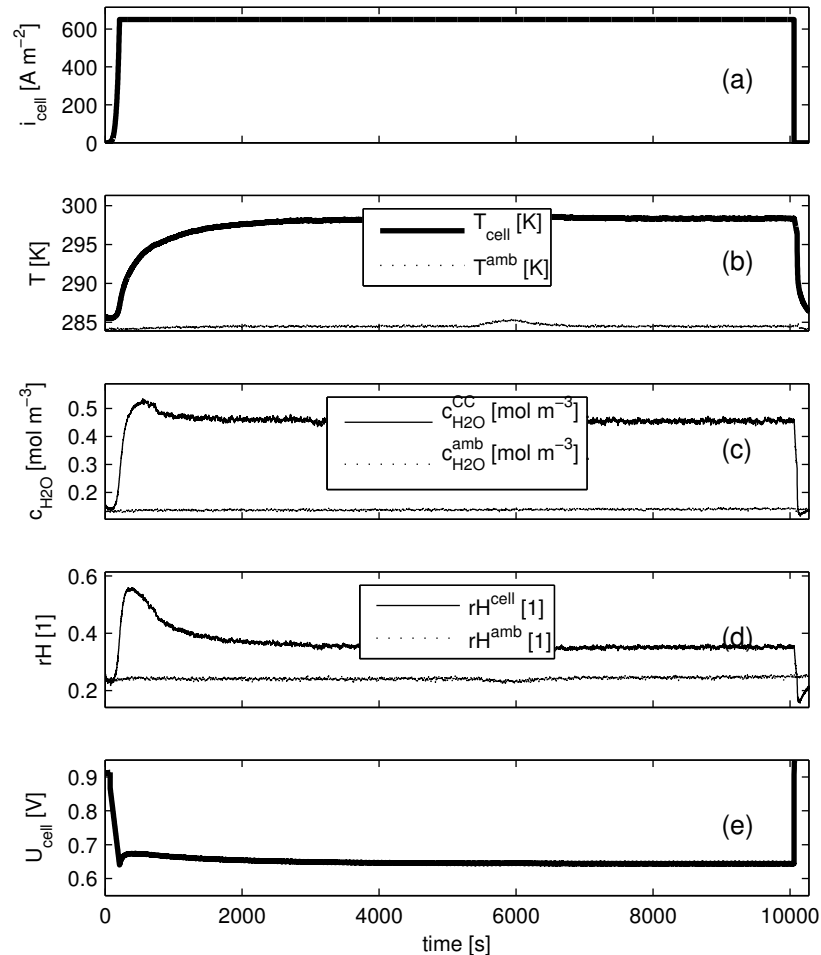


Figure 6: Measurement of the system response to a current density step. Measurement setup as described in [13]. The airflow is kept constant; (a) current density (b) cell voltage (c) temperature (d) relative humidity (e) water vapor concentration. The presented data is for an experimental setup without external cooling.

#### 4 Development of a Control Scheme

In this section a global control algorithm is developed based on analysis of the phase portraits of the two-dimensional system (18), (25). Because there is only one manipulated variable – the airflow –, but two control variables – temperature and water content –, it is not possible to control both control variables simultaneously. Instead, the objective is to formulate a control algorithm that takes the system in some suboptimal way to the desired set point while avoiding critical system states. In the present case, critical system state mainly means a state where the humidity exceeds

1  
2  
3  
4  
5  
6  
7  
8 100 % and liquid water condensation occurs. Since the open-loop system is already  
9 stable, stabilization by feedback is not required.

10 The control algorithm is developed in three steps. First, the dynamic behavior of  
11 the system is analyzed by generalized phase portraits. This gives a deeper insight on  
12 the global effect of different airflows. In the second step, a suitable steady state set  
13 point is chosen. Again due to the single manipulated variable, the set point cannot be  
14 chosen arbitrarily, but has to be feasible in the sense that there must be some constant  
15 airflow leading to this steady state. The third step consists in the design of a  
16 controller. The control algorithm should be simple enough for implementation on a  
17 microcontroller. Further, it should be robust against model errors, as it is based on a  
18 simple qualitative model. These two points are more important than an excellent  
19 performance of the closed-loop system.

#### 20 21 **4.1 Analysis of the Airflow Influence by Generalized Phase** 22 **Portraits**

23 As the fuel cell model is of second order, its dynamic behavior can be visualized  
24 conveniently by phase portraits. However, a classical phase portrait constructed for a  
25 single value of the airflow is not very useful for controller design. Instead one is  
26 interested to know how choosing a specific airflow value determines the time-  
27 derivatives of the system states and thus the “moving direction” of the system in the  
28 state space. If one evaluates the system dynamics at one point in the state space for all  
29 possible airflow values, one gets all directions the system can be forced to move,  
30 starting from this system state. Such an analysis is depicted in Figure 7. Figure 7  
31 shows the angles of direction in which the system can move from different positions  
32 in the state space. One should distinguish the ideal case of an unlimited airflow  
33 between zero and infinity and the realistic case of an airflow in a certain interval. The  
34 lower bound of this interval is defined by the fuel cell's oxygen demand. Oxygen  
35 depletion reduces the efficiency of the fuel cell. Therefore the airflow is chosen to  
36 always be greater than is necessary for an oxygen stoichiometric factor of three. The  
37 upper bound is given by the fact that the blower can only produce a limited maximal  
38 airflow. The influence of the restricted and the unrestricted choice of the airflow on  
39 the system is indicated in Figure 7 by dark grey and light grey respectively. Figure 7  
40 can be used to choose feasible steady state operation points and to construct  
41 trajectories that lead to these desired operation points without entering the forbidden  
42 shaded area where condensation occurs. For example, it can be seen that –  
43 independent of the chosen control algorithm – a limited airflow is not able to prevent  
44 condensation for certain states at low temperatures below 295 K. This is because  
45 trajectories starting at points close to the shaded forbidden area always point into that  
46 area, no matter what airflow is chosen. If one wants to avoid condensation at low  
47 temperatures, one can do that by increasing the maximum power of the blower. On  
48 the other hand, if the cell temperature is sufficiently high, above about 305 K, then it  
49 will always be possible to avoid condensation by suitable control.

50  
51  
52  
53  
54  
55  
56  
57  
58  
59  
60

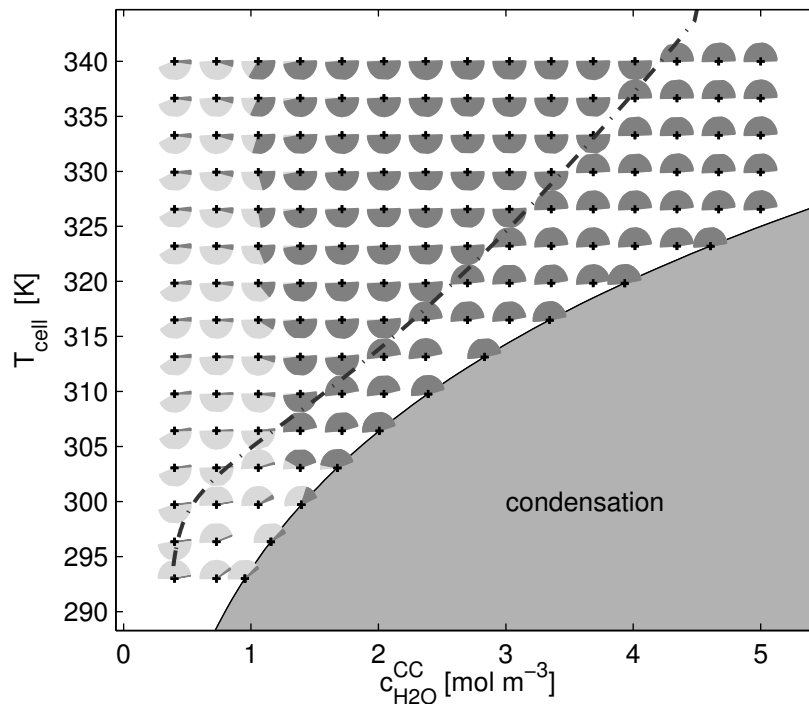


Figure 7: Possible directions of trajectories for an unlimited maximal inlet airflow  $0.0016 \text{ mol s}^{-1} \leq F^{\text{in,CC}}$  (light grey) and for a limited maximal airflow  $0.0016 \text{ mol s}^{-1} \leq F^{\text{in,CC}} \leq 0.01 \text{ mol s}^{-1}$  (dark grey). Full circular areas around the starting points (+) would represent ideal influence on the system. The current density is fixed at  $i_{\text{cell}} = 4000 \text{ A m}^{-2}$ . The dash-dotted line marks feasible steady-state set points.

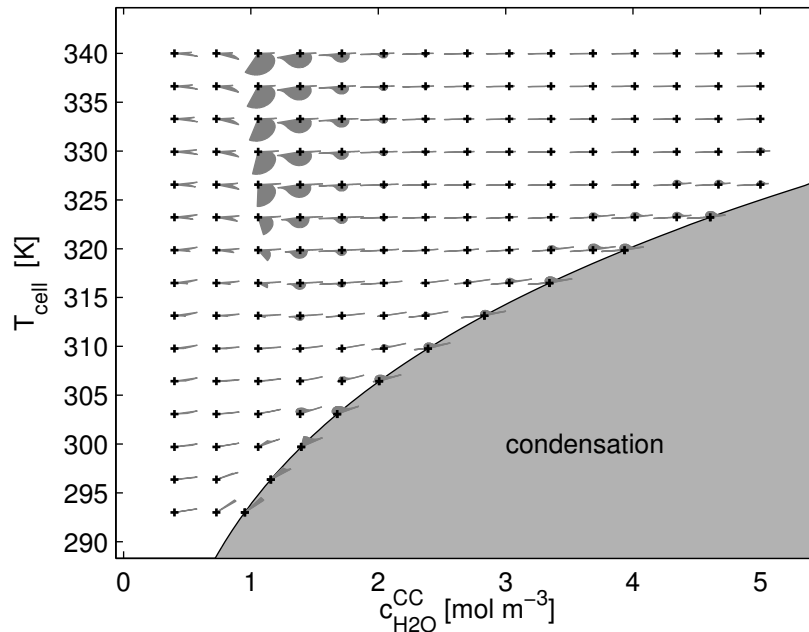


Figure 8: Possible directions of trajectories (see Figure 7) rated with the respective speed of change. The values at each point (+) are normalized to the maximal speed at this point. In general, changes of the water vapor concentration are faster than changes of the temperature.

Figure 8 shows the possible moving directions of the system analogously to Figure 7 but with the additional information of the speed of change for all possible directions. The speed of change is computed by

$$v = \left\| \frac{dx}{dt} \right\| = \sqrt{\left( \frac{1}{c_{\text{H}_2\text{O},\text{scal}}^{\text{CC}}} \frac{dc_{\text{H}_2\text{O}}^{\text{CC}}}{dt} \right)^2 + \left( \frac{1}{T_{\text{cell},\text{scal}}} \frac{dT_{\text{cell}}}{dt} \right)^2} \quad (28)$$

and deforms the circular area segments of Figure 7. It can be seen in Figure 8 that changes of the water vapor concentration are much faster than changes of the temperature. This can be explained by the bigger storage capacities for heat than for water in the system.

## 4.2 Choice of Steady State Set Points

Figure 7 also indicates feasible steady state set points. These are the points on the dash-dotted line where the opening of the grey segments flips from top to bottom.

One can in principle choose any point on this line as set point. As Figure 7 is valid only for one fixed cell current, the line of feasible set points will shift if the electric

load changes. For the following studies, a set point has been chosen that is feasible for a range of currents.

For practical purposes it is often sufficient to keep the system states in a region around the operation point. This operation window is indicated by a light grey rectangular area in the following Figures.

### 4.3 Choosing the Locally Best Airflow

As first step towards the final control algorithm, a rather simple approach is tested. The idea is always to choose the airflow that provides the fastest approach to the set point in the current state. The speed of approach is defined here as the negative change of the squared distance to the center of the operation window and computed as follows.

$$\begin{aligned} v &= -\frac{1}{2} \frac{d}{dt} \left( \left( \frac{\Delta c_{\text{H}_2\text{O}}^{\text{CC}}}{c_{\text{H}_2\text{O},\text{scal}}^{\text{CC}}} \right)^2 + \left( \frac{\Delta T_{\text{cell}}}{T_{\text{cell},\text{scal}}} \right)^2 \right) \\ &= -\frac{\Delta c_{\text{H}_2\text{O}}^{\text{CC}}}{\left(c_{\text{H}_2\text{O},\text{scal}}^{\text{CC}}\right)^2} \frac{dc_{\text{H}_2\text{O}}^{\text{CC}}}{dt} - \frac{\Delta T_{\text{cell}}}{\left(T_{\text{cell},\text{scal}}\right)^2} \frac{dT_{\text{cell}}}{dt} \end{aligned} \quad (29)$$

$$\Delta c_{\text{H}_2\text{O}}^{\text{CC}} = c_{\text{H}_2\text{O}}^{\text{CC}} - c_{\text{H}_2\text{O}}^{\text{CC, setcenter}}, \quad \Delta T_{\text{cell}} = T_{\text{cell}} - T_{\text{cell}}^{\text{setcenter}}$$

At each point in the state space, the optimal airflow is chosen that maximizes  $v$  in (29). The result is given in Figure 9. One can see several things from this diagram. First, the simple approach is able to take the system from nearly arbitrary initial states to the desired operation window marked by the grey box. The only exceptions are initial states with a low temperature and high humidity, where the blower is too weak to prevent condensation. The second point is that the air blower nearly always operates on minimum or maximum power. If the temperature is too high, the airflow is set to a maximum to cool down the system. If the temperature is too low, the minimum airflow is chosen in order to accumulate reaction heat. This rule is broken only at the border to the condensation area, where a high airflow is needed to blow out redundant water. If the temperature is on the desired level one can increase humidity by a small airflow or decrease it by a high airflow. The qualitative behavior shown in Figure 9 does hardly change for different parameter sets and operation windows. These deviations inspire an even simpler control algorithm presented in the following.

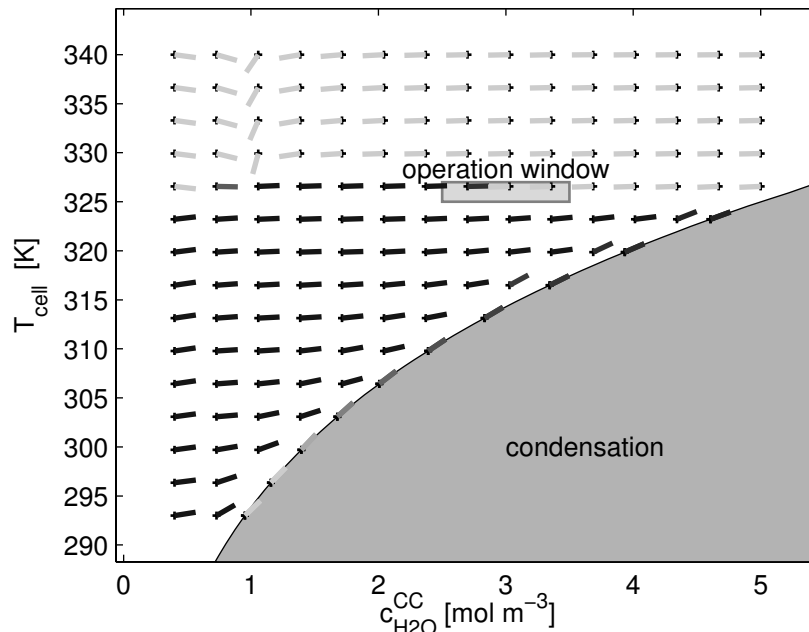


Figure 9: Direction of the maximal speed of change towards the operation point. The respective inlet airflow  $F^{\text{in,CC}}$  is indicated by the color spanning from dark grey for minimal airflow to light grey for maximal airflow.

#### 4.4 Formulation of the Control Algorithm

Based on the results of the previous section, a simple control algorithm is proposed for the miniature fuel cell stack:

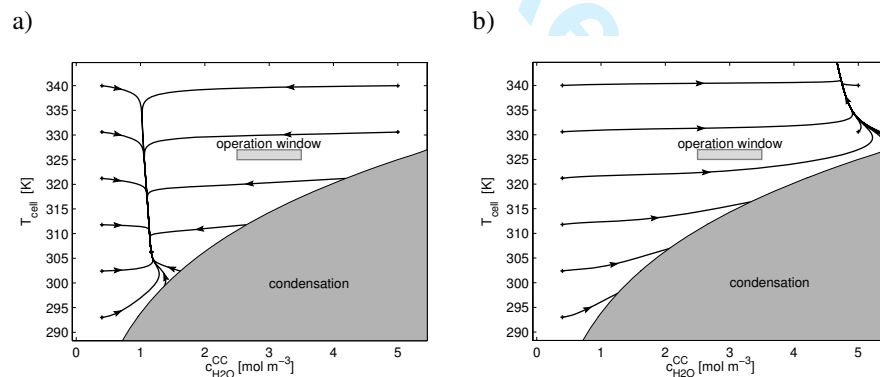
- Rule 1: If the system is “above” or “right” of the operation window, apply the maximal airflow.
- Rule 2: If the system is “below” or “left” of the operation window, apply the minimal airflow.
- Rule 3: If the relative humidity violates an upper threshold, apply the maximal airflow. This rule overrides the second rule.

For implementation the regions have to be described in terms of cell temperature and water vapor concentration. Less than the maximal airflow may be sufficient to prevent the fuel cell from flooding, but since quantitative values are not known the maximum is the safest value to choose. Additionally, linear transition zones are defined between regions with different airflows to prevent chattering. Rapid changes of the airflow cannot be realized because of the inertia of the blower and the air itself. This problem is reduced by continuously changing the airflow.

The control algorithm can be expressed in terms of cell temperature and water vapor concentration by the following relations. The linear transition zones are left out here for the sake of readability. The operation window is characterized by the parameters  $T^{\text{set}}$  and  $c_{\text{H}_2\text{O}}^{\text{CC,set}}$  which both describe intervals with maximal and minimal acceptable values.

$$\begin{aligned}
 F_{C1}^{in,CC} &= \begin{cases} F_{max} & \left( (T_{cell} > T^{set,max}) \vee \left( (T_{cell} > T^{set,max}) \wedge (c_{H_2O}^{CC} > c_{H_2O}^{CC,set,max}) \right) \right) \\ F_{min} & \left( (T_{cell} < T^{set,min}) \vee \left( (T_{cell} < T^{set,min}) \wedge (c_{H_2O}^{CC} < c_{H_2O}^{CC,set,min}) \right) \right) \\ F_{nom} & \text{else} \end{cases} \\
 F_{C2}^{in,CC} &= \begin{cases} F_{max} & (rH^{cell} \geq rH_{max}) \\ F_{min} & (rH^{cell} < rH_{min}) \end{cases} \\
 F_{Controller}^{in,CC} &= \max(F_{C1}^{in,CC}, F_{C2}^{in,CC})
 \end{aligned} \tag{30}$$

A graphical representation of the control algorithm is shown in Figure 10c. The resulting trajectories of the closed-loop system (Figure 10d) lead to the operation window and are composed of trajectories relating to the maximal and minimal airflow (Figures 10a and 10b) in the respective regions as well as trajectory parts that lie in the region boundaries. Inside the operation window a nominal airflow is applied that keeps the system at the operation point. For practical application this value can be obtained from steady-state measurements.



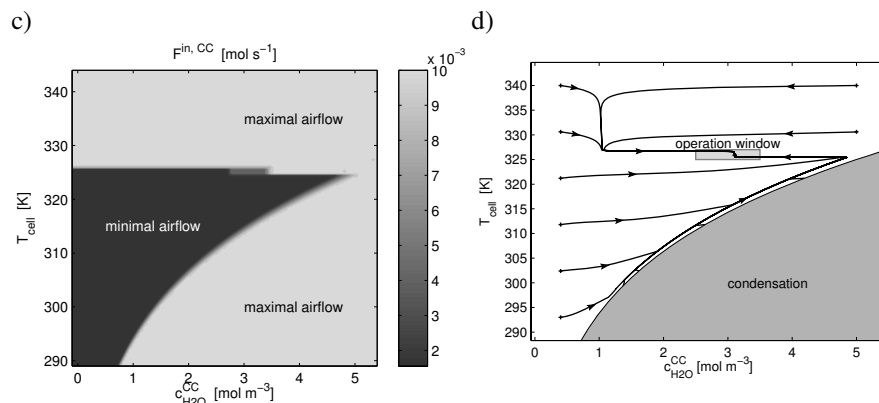


Figure 10: a) and b) show the phase portraits for the maximal and the minimal airflow respectively. The light grey area marks the operation window. c) Graphical representation of the control algorithm. The applied airflow depends only on the system states. d) The trajectories of the closed-loop system. The current density is fixed at  $i_{\text{cell}} = 4000 \text{ A m}^{-2}$ .

In summary, the problem of two control variables and one manipulated variable is solved by focusing on the temperature in most cases. Only when the humidity in the cell becomes critical or when the temperature has the nominal value, the airflow is used to control the water concentration. The reason for the success of this strategy lies in the different time constants of the water and the energy balance. As the dynamics of the water concentration are very fast, one can quickly adjust the water concentration without disturbing the temperature strongly.

The proposed control algorithm is very simple. The rules depend only on the current states of the system. The implementation on a microcontroller should therefore pose no problem. The demands on sensor equipment are also modest, as only a temperature and a humidity measurement are required.

## 5 Conclusions

In the present work a controller has been designed that adjusts temperature and humidity of a miniaturized fuel cell system by using the airflow of a blower as a single manipulated variable. The controller design is based on a phase plane analysis of a qualitative fuel cell model. The resulting controller is simple and easy to implement. It only needs measurement information that is readily available in a miniature fuel cell stack. The control law relies mainly on the qualitative properties of the model, and therefore should be robust against model errors.

It has been shown that the controller is able to take the system from a rather large region of attraction to the desired operation window. Limitations exist for low fuel cell temperatures, where it may be hard to heat up the stack and to prevent condensation simultaneously. These difficulties may be overcome by modifications of the system design like a stronger air-blower. Another alternative might be to use the cell current as an additional manipulated variable, if permitted by the actual application.

## References

- [1] M. A. Danzer, J. Wilhelm, H. Aschemann, and E. P. Hofer. *Journal of Power Sources*, **2008**, 176 (2), 515–522
- [2] J. Golbert and D. R. Lewin. *Journal of Power Sources*, **2004**, 135 (1-2), 135–151
- [3] M. Grujicic, K. Chittajallu, and J. Pukrushpan. *Proceedings of the Institution of Mechanical Engineers Part D- Journal of Automobile Engineering*, **2004**, 218 (A7), 1239–1250
- [4] R. Hanke-Rauschenbach, M. Mangold, and K. Sundmacher. *Journal of the Electrochemical Society*, **2008**, 155 (2), B97–B107
- [5] A. Y. Karnik, J. Sun, A. G. Stefanopoulou, and J. H. Buckland. *IEEE Transactions On Control Systems*, **2009**, 17 (2), 283–297
- [6] K. C. Lauzze and D. J. Chmielewski. *Industrial & Engineering Chemistry Research*, **2006**, 45 (13), 4661–4670
- [7] W. K. Na and B. Gou. *IEEE Transactions on Energy*, **2008**, 23 (1), 179–190
- [8] W. Neubrand. *Ph.D. Thesis*, Universität Stuttgart, Germany, **1999**
- [9] J. Niemeyer. *Ph.D. Thesis*, Universität Karlsruhe (TH), Germany, **2008**
- [10] J. T. Pukrushpan. *Ph.D. Thesis*, The University of Michigan, USA, **2003**
- [11] J. O. Schumacher, P. Gemmar, M. Denne, M. Zedda, and M. Stueber. *Journal of Power Sources*, 2004, 129, 143–151
- [12] E. Shkolnikov, M. Vlaskin, A. Iljukhin, A. Zhuk, and A. Sheindlin. *Journal of Power Sources*, **2008**, 185, 967–972
- [13] M. Weiland. *Master's Thesis*, TU Berlin, Germany, **2008**
- [14] M. Wöhr. *Ph.D. Thesis*, Universität Stuttgart, Germany, **2000**
- [15] F. Zenith and S. Skogestad. *Journal of Process Journal of Process Control*, **2009**, 19, 415–432

## Tables

Table 1: Symbols

Symbol	Description	Units
$A_{\text{cell}}$	active reaction area of a single cell	$\text{m}^2$
$c_{\alpha}$	concentration of species $\alpha$	$\text{mol m}^3$
$c_{p,\text{gas}}$	heat capacity of cathode side gas	$\text{J mol}^{-1} \text{K}^{-1}$
$C_{p,\text{solid}}$	heat capacity of the solid parts of the fuel cell stack	$\text{J K}^{-1}$
$n$	number of single fuel cells in the stack	-
$F$	molar flow	$\text{mol s}^{-1}$
$F$	Faraday constant	$96485 \text{ C mol}^{-1}$
$F^{\text{ext}}$	external airflow	$\text{mol s}^{-1}$
$h$	thickness	m
$\dot{H}$	enthalpy flow	$\text{J s}^{-1}$

$i$	current density	$\text{A m}^{-2}$
$i^0$	exchange current density	$\text{A m}^{-2}$
$k_{\text{env}}$	heat transfer coefficient between the fuel cell stack and the environment	$\text{W K}^{-1}$
$p$	pressure	Pa
$p_{\text{sat}}$	saturation pressure of water vapor	Pa
$P_{\text{el}}$	electrical power	W
$Q_{\text{th}}$	heat flow	W
$R$	ideal gas constant	$8.314 \text{ J mol}^{-1} \text{ K}^{-1}$
$R_{\text{cell}}$	ohmic resistance of a single cell	$\Omega$
$rH$	relative humidity	-
$T$	temperature	K
$U_{\text{cell}}^0$	open circuit voltage of a single cell	V
$U_{\text{cell}}$	voltage of a single cell	V
$U_{\text{th}}$	heating value voltage of a single cell	V
$V$	volume	$\text{m}^3$
$x_{\alpha}$	mole fraction of species $\alpha$	-
$z$	electron transfer number	2
$\alpha$	symmetry factor	-
$\Delta_r H^\theta$	reaction enthalpy at $25^\circ\text{C}$ , 1 bar	$\text{J mol}^{-1}$
$\Delta_r G^\theta$	free reaction enthalpy at $25^\circ\text{C}$ , 1 bar	$\text{J mol}^{-1}$
$\Delta\phi$	electrical potential difference	V
$\eta$	overvoltage	V
$\kappa$	specific conductivity	$\text{S m}^{-1}$

Table 2: Indices

Symbol	Description
A	anode
AC	anode gas channels
amb	ambient
C	cathode
CC	cathode gas channels
ext	outside the fuel cell stack
gas	gas phase
in	inlet
M	membrane

out	outlet
ss	steady state
ref	reference conditions

Table 3: Parameters

Symbol	Value	Source
$A_{\text{cell}}$	$10^{-4} \text{ m}^2$	Fraunhofer IZM Berlin
$c_{\text{H}_2\text{O},\text{scal}}^{\text{CC}}$	$1 \text{ mol m}^{-3}$	-
$c_{p,\text{gas}}$	$30 \text{ J K}^{-1} \text{ mol}^{-1}$	-
$C_{p,\text{solid}}$	$60 \text{ J K}^{-1} (64 \text{ J K}^{-1})^*$	-
$F^{\text{ext}} / F^{\text{in,CC}}$	$25 (0)^*$	-
$F^{\text{max}}$	$0.01 \text{ mol s}^{-1}$	-
$h_{\text{M}}$	$18 \cdot 10^{-6} \text{ m}$	Fraunhofer IZM Berlin
$i_{\text{cell}}$	$4000 \text{ A m}^{-2}$	-
$k_{\text{env}}$	$0.08 \text{ W K}^{-1} *$	-
$n$	$10 (6)^*$	Fraunhofer IZM Berlin
$p^{\text{CC}}$	$10^5 \text{ Pa}$	Fraunhofer IZM Berlin
$rH^{\text{amb}}$	$0.4$	-
$R_{\text{cell}}$	$0.01 \Omega$	Fraunhofer IZM Berlin
$T^{\text{amb}}$	$293.15 \text{ K}$	-
$T_{\text{cell,scal}}$	$1 \text{ K}$	-
$V_{\text{CC}}/n$	$1.7 \cdot 10^{-6} \text{ m}^3$	Fraunhofer IZM Berlin
$\Delta_r G^\theta$	$-228.6 \cdot 10^3 \text{ J mol}^{-1}$	-
$\Delta_r H^\theta$	$-241.8 \cdot 10^3 \text{ J mol}^{-1}$	-
	* Figure 5	
membrane model		
$M_{\text{H}_2\text{O}}$	$0.018 \text{ kg mol}^{-1}$	[8]
$\rho_{\text{H}_2\text{O}}$	$1000 \text{ kg m}^{-3}$	[8]
$\rho_{\text{M}}^{\text{dry}}$	$2050 \text{ kg m}^{-3}$	[8]
$X^{\text{dry}}$	$0.909 \text{ mol}_{\text{SO}_3} \text{ kg}^{-1}$	[8]
reaction kinetics		
$c_{\text{O}_2}^{\text{ref}}$	$172.6 \text{ mol m}^{-3}$	[14]
$E_{\text{a}}^{\text{C}}$	$28 \cdot 10^3 \text{ J mol}^{-1}$	[14]

$i^{0,\text{ref,C}}$	$1.12 \cdot 10^{-2} \text{ A m}^{-2}$	[14]
$T^{\text{ref}}$	353 K	[14]
$\alpha^{\text{C}}$	0.5	[14]

## Figure Captions

Figure 1: Scheme of the airflow in the fuel cell system. The light grey area in the center represents the fuel cell stack.	3
Figure 2: Basic configuration of a H <sub>2</sub> -PEMFC with a) gas channels b) gas diffusion layers c) electrodes and d) the membrane. The anode side is operated in dead-end mode here.	4
Figure 3: Stationary solutions for the variation of the current density. The airflow is kept constant at $F^{\text{in,CC}} = 0.0023 \text{ mol s}^{-1}$ . (a) water vapor concentration (b) temperature (c) partial pressure and saturation pressure of water vapor (d) relative humidity (e) cell voltage.	12
Figure 4: Stationary impedance values for varied current densities. (left) simulation, membrane impedance only, (right) measurement of the whole system. Measurement setup as described in [13]. The airflow is kept constant. The minimum impedance corresponds to a maximum of humidification as shown in Figure 3d.	13
Figure 5: System response to a current density step. The airflow is kept constant at $F^{\text{in,CC}} = 0.0024 \text{ mol s}^{-1}$ ; (a) current density (b) cell voltage (c) temperature (d) relative humidity (e) water vapor concentration. The overshoot of the relative humidity is due to slower dynamics of the temperature compared to the water vapor concentration. On the falling slope of the humidity water is released from the membrane. This also leads to an overshoot of the water vapor concentration.	14
Figure 6: Measurement of the system response to a current density step. Measurement setup as described in [13]. The airflow is kept constant; (a) current density (b) cell voltage (c) temperature (d) relative humidity (e) water vapor concentration. The presented data is for an experimental setup without external cooling.	15
Figure 7: Possible directions of trajectories for an unlimited maximal inlet airflow $0.0016 \text{ mol s}^{-1} \leq F^{\text{in,CC}}$ (light grey) and for a limited maximal airflow $0.0016 \text{ mol s}^{-1} \leq F^{\text{in,CC}} \leq 0.01 \text{ mol s}^{-1}$ (dark grey). Full circular areas around the starting points (+) would represent ideal influence on the system. The current density is fixed at $i_{\text{cell}} = 4000 \text{ A m}^{-2}$ . The dash-dotted line marks feasible steady-state set points.	17
Figure 8: Possible directions of trajectories (see Figure 7) rated with the respective speed of change. The values at each point (+) are normalized to the	18

maximal speed at this point. In general, changes of the water vapor concentration are faster than changes of the temperature.	
Figure 9: Direction of the maximal speed of change towards the operation point. The respective inlet airflow $F^{\text{in,CC}}$ is indicated by the color spanning from dark grey for minimal airflow to light grey for maximal airflow.	20
Figure 10: a) and b) show the phase portraits for the maximal and the minimal airflow respectively. The light grey area marks the operation window. c) Graphical representation of the control algorithm. The applied airflow depends only on the system states. d) The trajectories of the closed-loop system. The current density is fixed at $i_{\text{cell}} = 4000 \text{ A m}^{-2}$ .	22

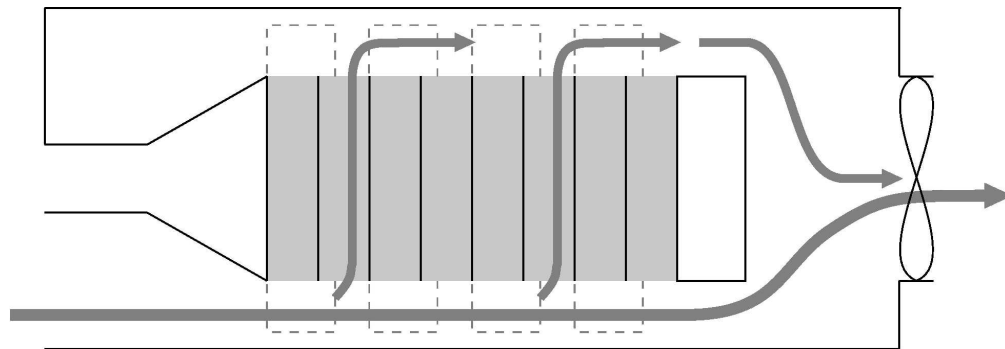


Figure 1: scheme of airflow  
165x56mm (600 x 600 DPI)

cr Peer Review

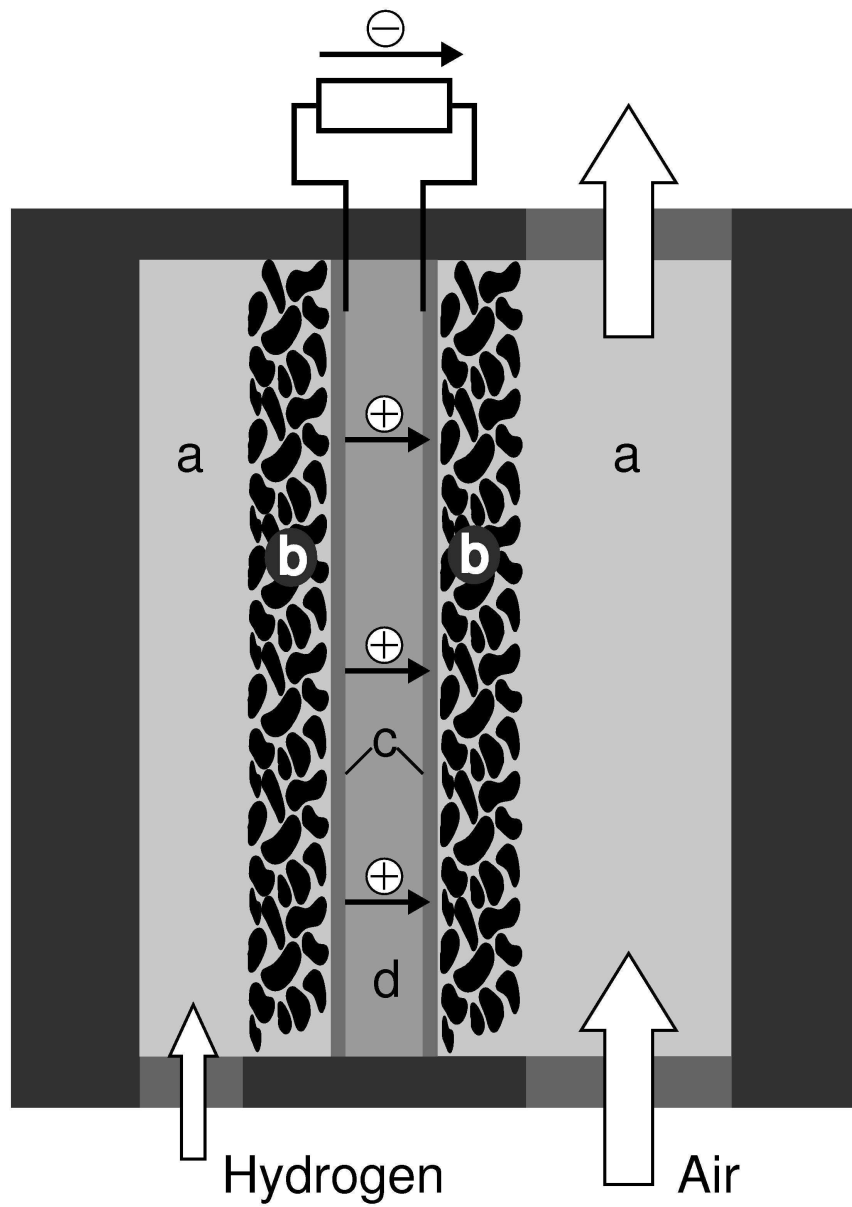


Figure 2: Basic configuration of a PEMFC  
93x131mm (600 x 600 DPI)

1  
2  
3  
4  
5  
6  
7  
8  
9  
10  
11  
12  
13  
14  
15  
16  
17  
18  
19  
20  
21  
22  
23  
24  
25  
26  
27  
28  
29  
30  
31  
32  
33  
34  
35  
36  
37  
38  
39  
40  
41  
42  
43  
44  
45  
46  
47  
48  
49  
50  
51  
52  
53  
54  
55  
56  
57  
58  
59  
60

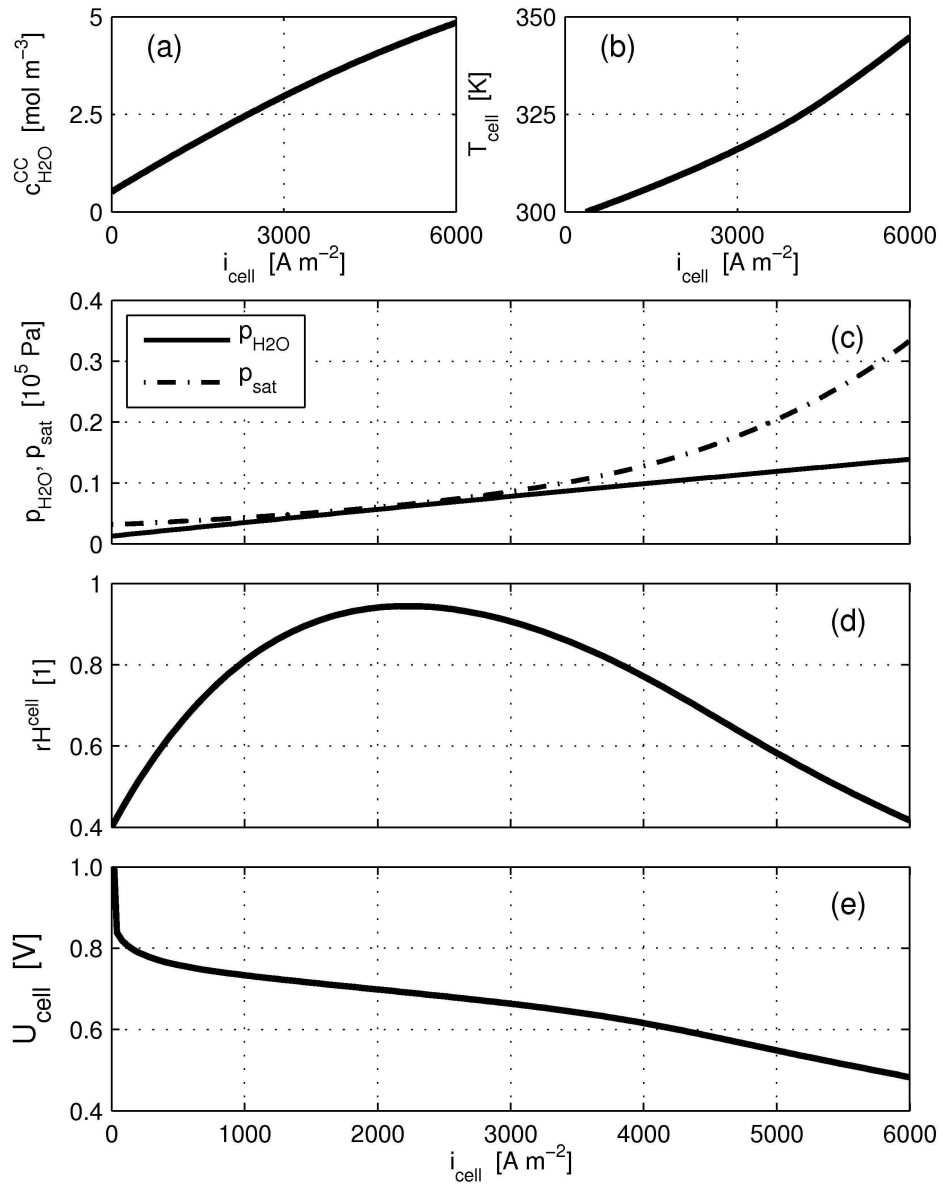
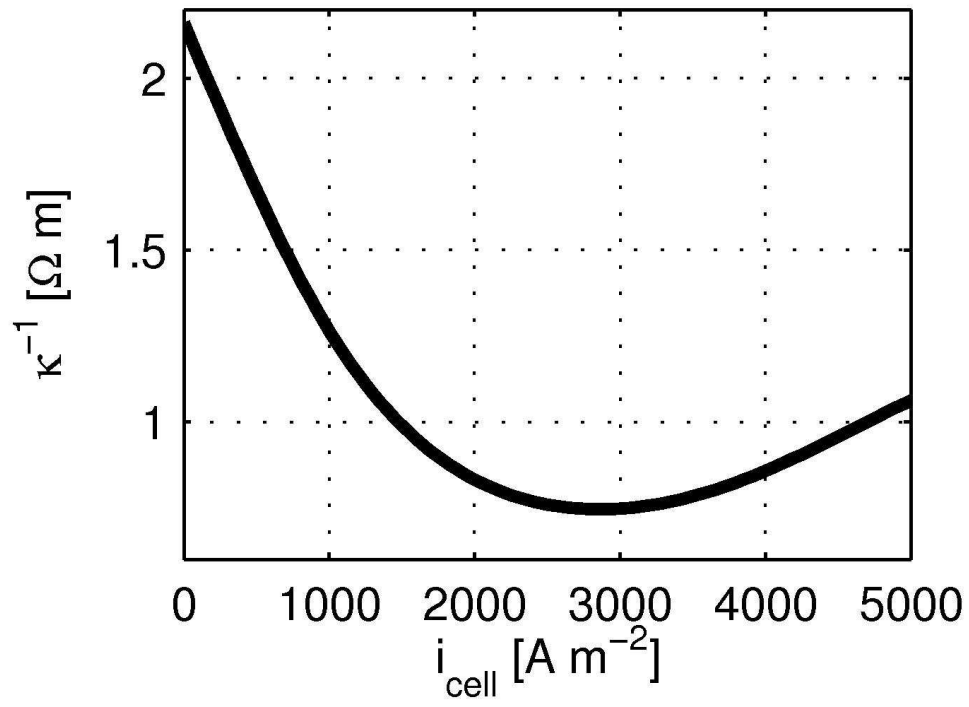
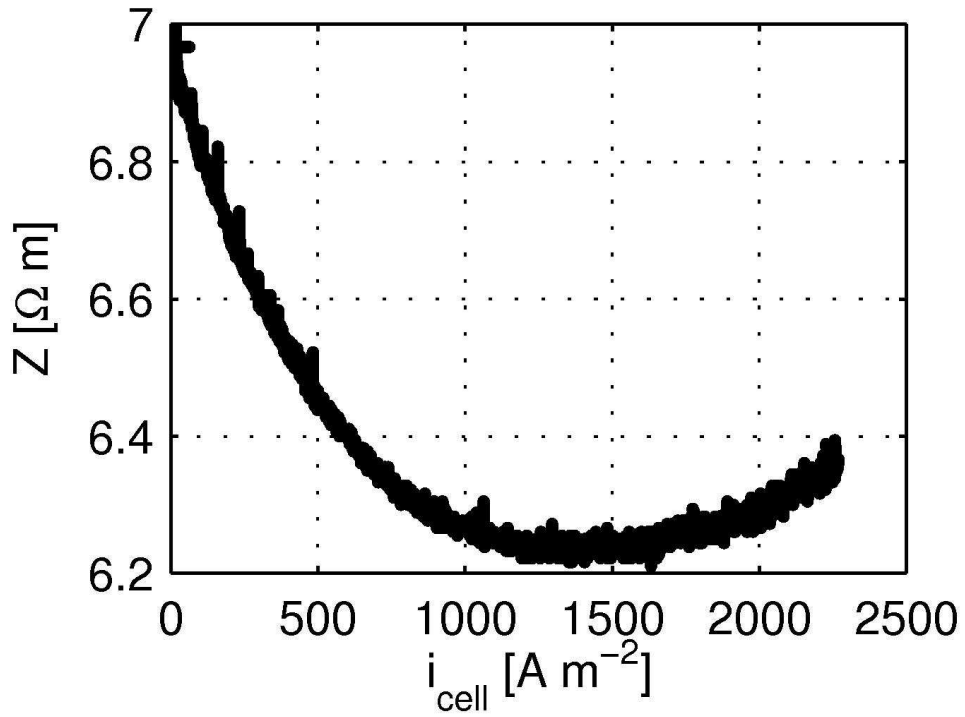


Figure 3: stationary solutions for the variation of the current density  
110x139mm (600 x 600 DPI)



59x45mm (600 x 600 DPI)

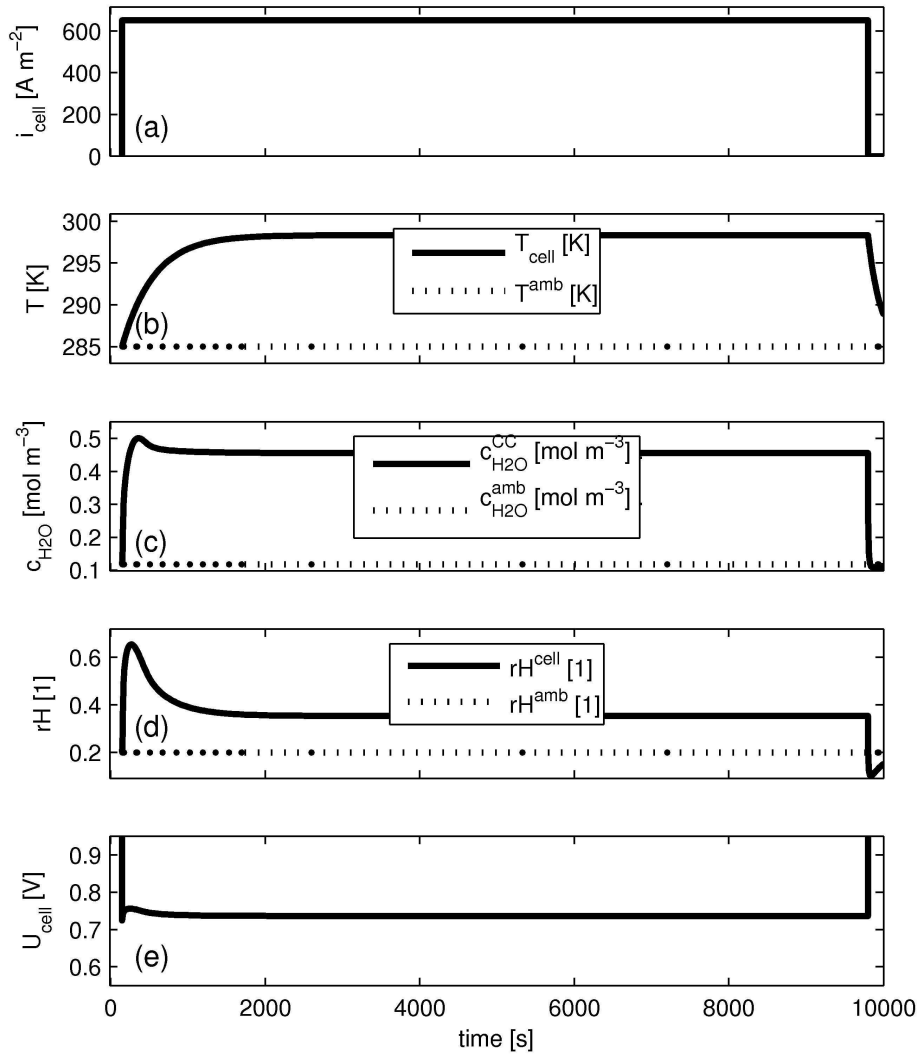
Review



59x45mm (600 x 600 DPI)

Review

1  
2  
3  
4  
5  
6  
7  
8  
9  
10  
11  
12  
13  
14  
15  
16  
17  
18  
19  
20  
21  
22  
23  
24  
25  
26  
27  
28  
29  
30  
31  
32  
33  
34  
35  
36  
37  
38  
39  
40  
41  
42  
43  
44  
45  
46  
47  
48  
49  
50  
51  
52  
53  
54  
55  
56  
57  
58  
59  
60



119x144mm (600 x 600 DPI)

1  
2  
3  
4  
5  
6  
7  
8  
9  
10  
11  
12  
13  
14  
15  
16  
17  
18  
19  
20  
21  
22  
23  
24  
25  
26  
27  
28  
29  
30  
31  
32  
33  
34  
35  
36  
37  
38  
39  
40  
41  
42  
43  
44  
45  
46  
47  
48  
49  
50  
51  
52  
53  
54  
55  
56  
57  
58  
59  
60

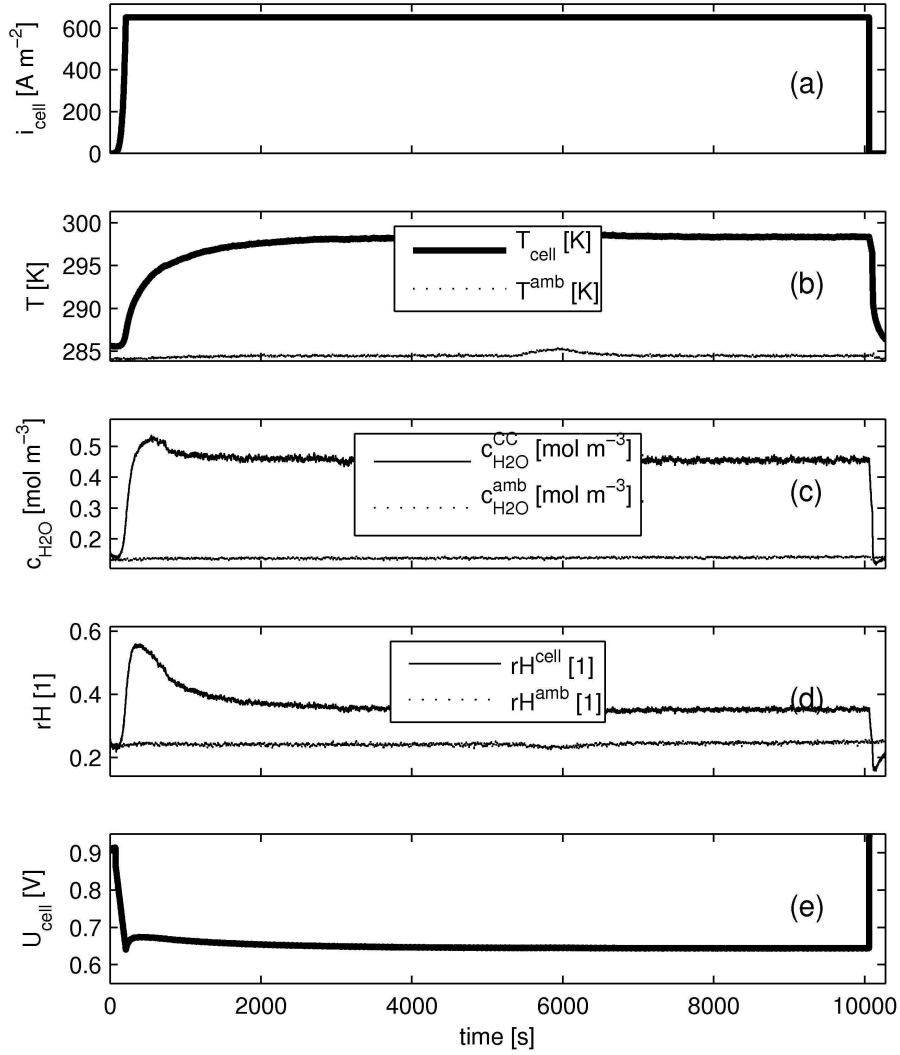


Figure 6: measurement of the system response to a current density step  
119x144mm (600 x 600 DPI)

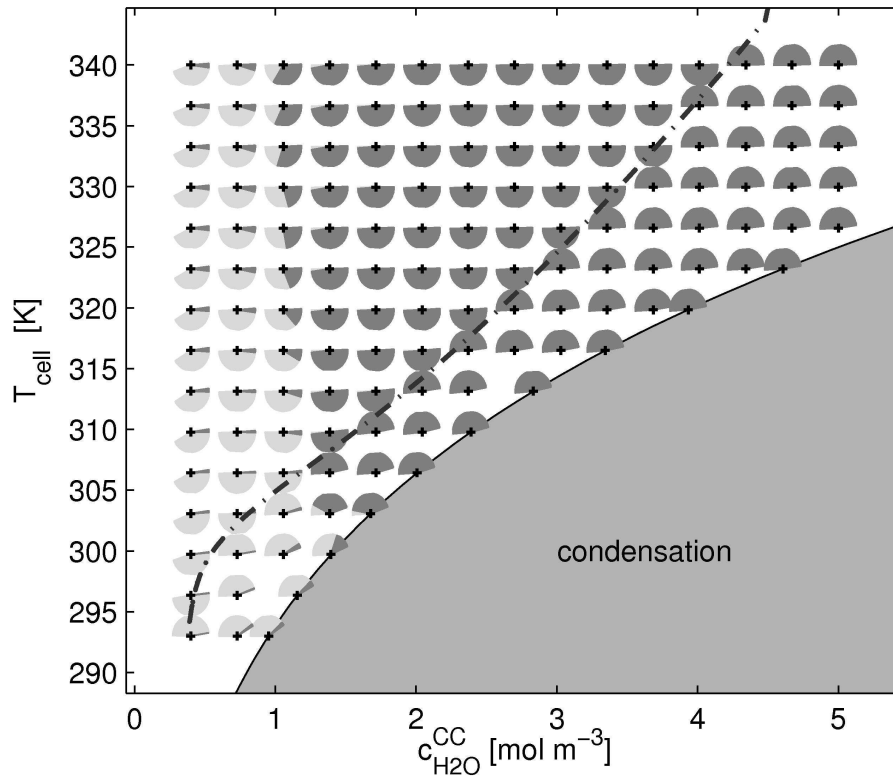


Figure 7: Possible directions of trajectories for an unlimited maximal inlet airflow 119x100mm (600 x 600 DPI)

iew

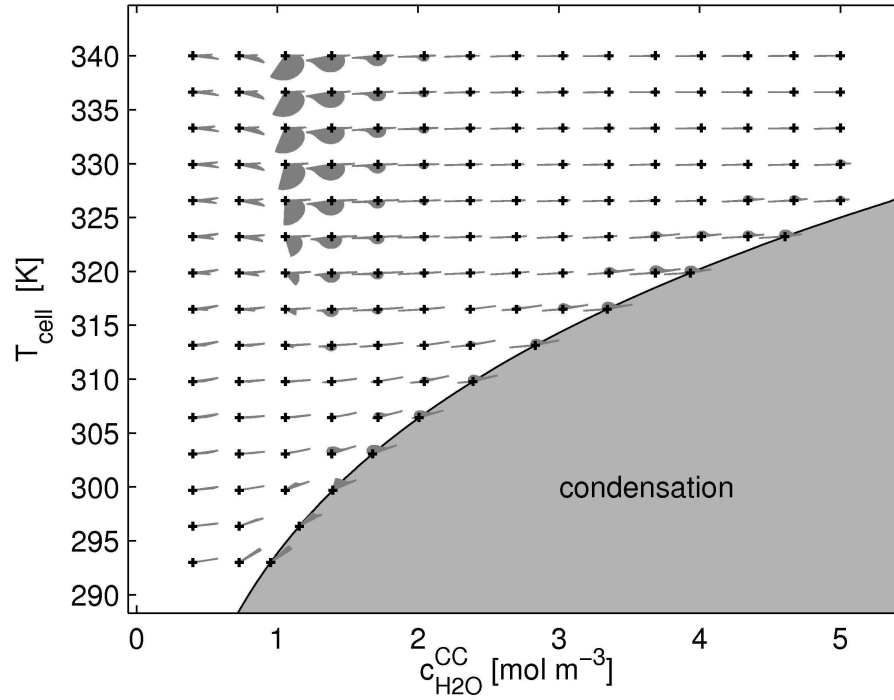


Figure 8: Possible directions of trajectories rated with the respective speed of change  
119x90mm (600 x 600 DPI)

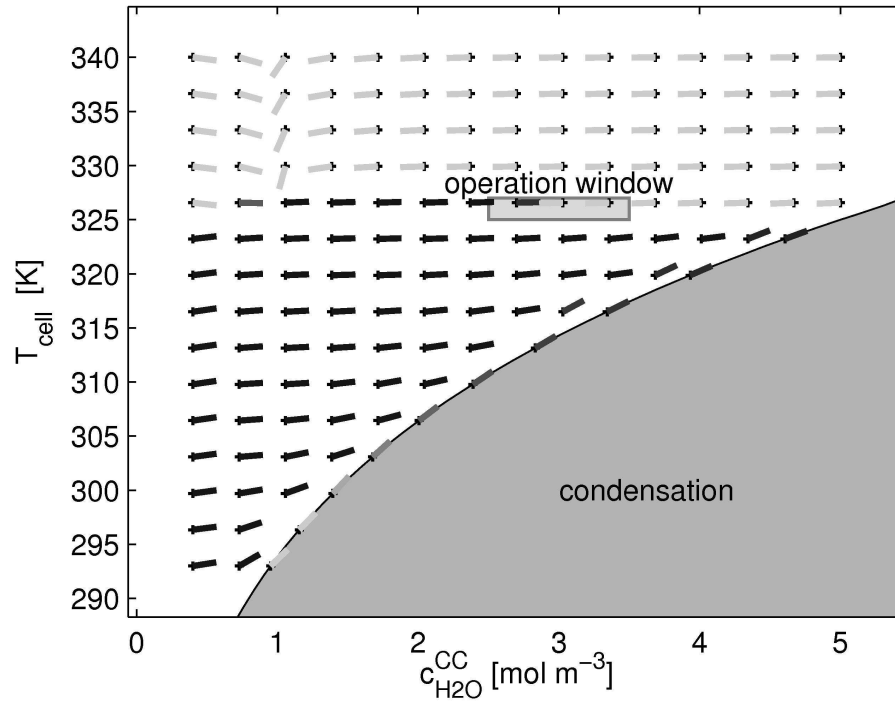


Figure 9: Direction of the maximal speed towards the operation point  
119x91mm (600 x 600 DPI)

Review

1  
2  
3  
4  
5  
6  
7  
8  
9  
10  
11  
12  
13  
14  
15  
16  
17  
18  
19  
20  
21  
22  
23  
24  
25  
26  
27  
28  
29  
30  
31  
32  
33  
34  
35  
36  
37  
38  
39  
40  
41  
42  
43  
44  
45  
46  
47  
48  
49  
50  
51  
52  
53  
54  
55  
56  
57  
58  
59  
60

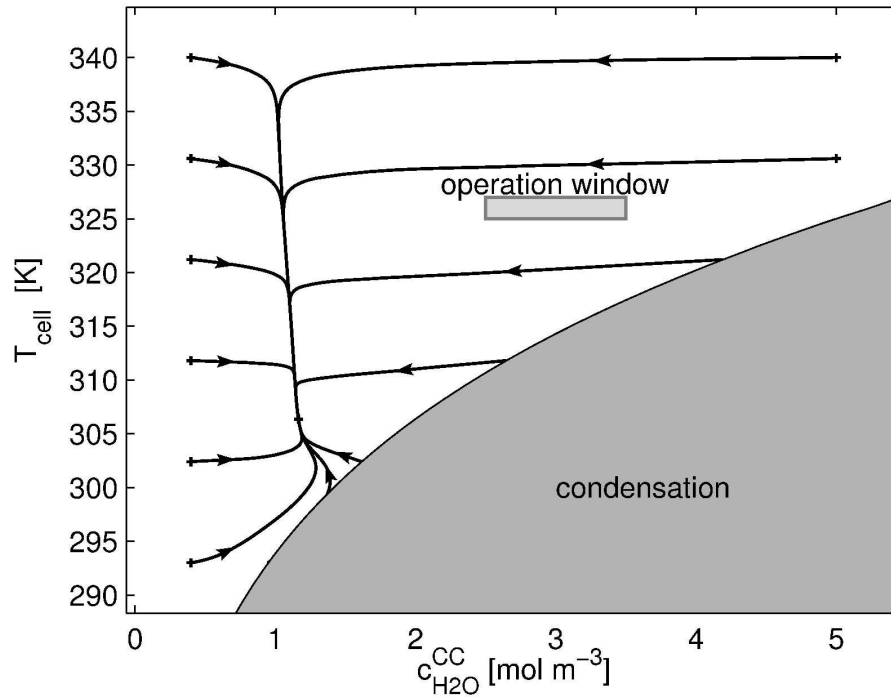


Figure 10 a: Phase portrait for maximal airflow  
150x113mm (600 x 600 DPI)

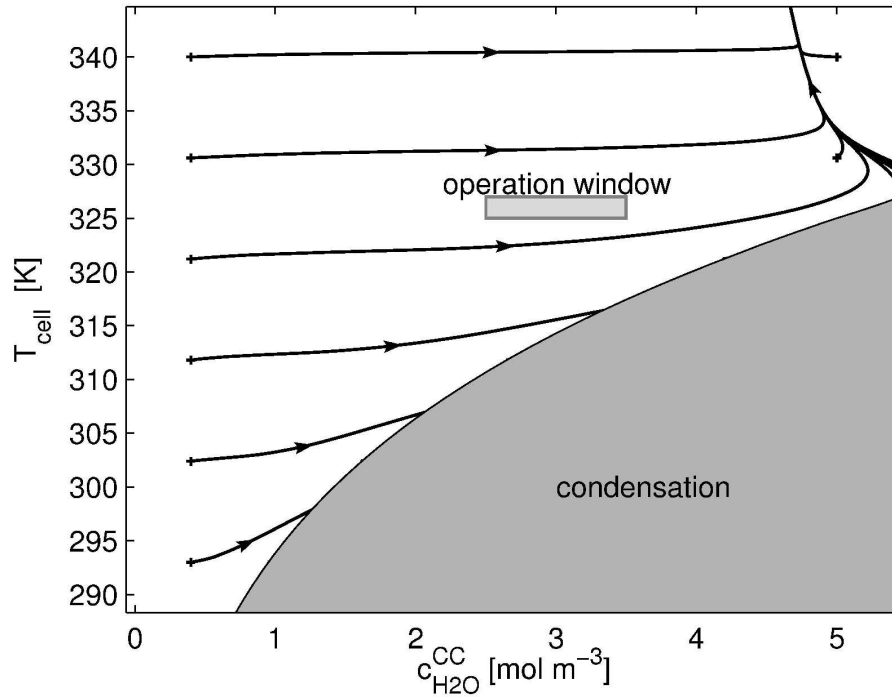


Figure 10 b: Phase portraits for minimal airflow  
150x113mm (600 x 600 DPI)

review

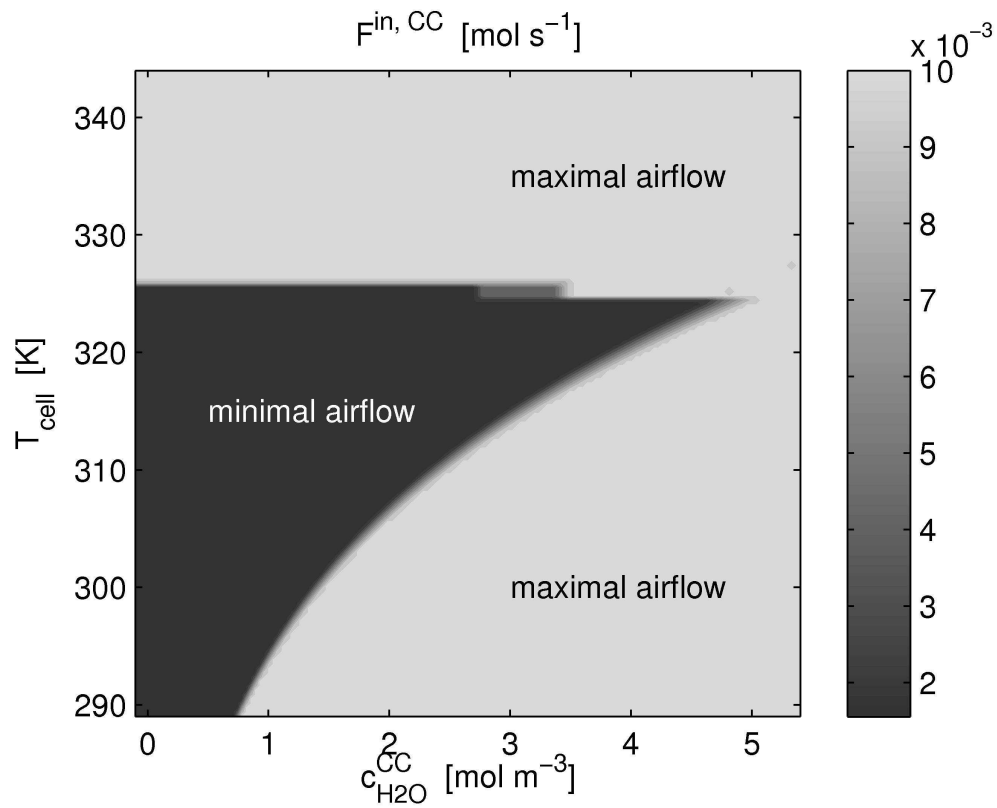


Figure 10 c: Graphical representation of the control algorithm  
112x91mm (600 x 600 DPI)

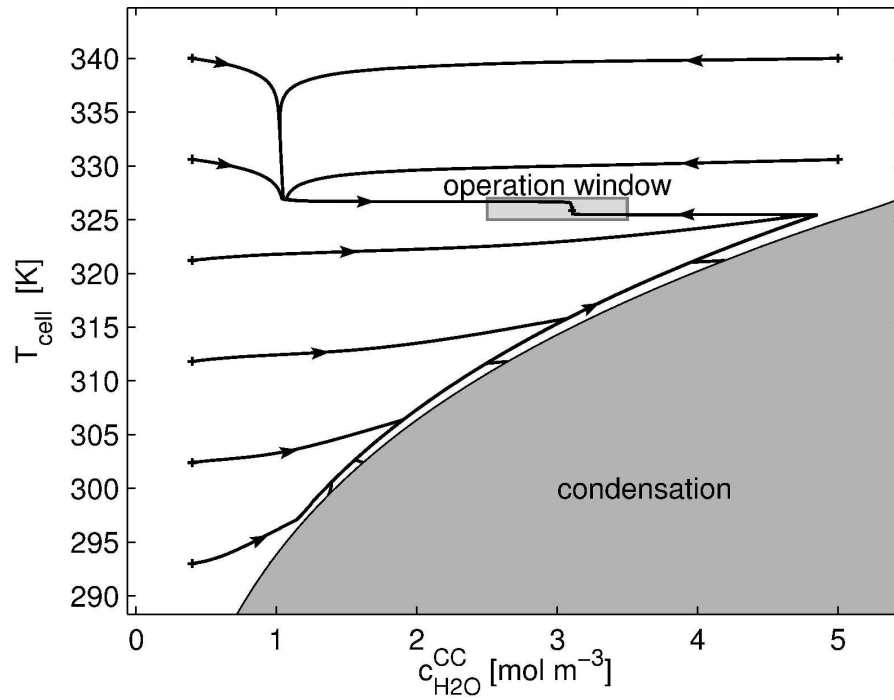


Figure 10 d: Trajectories of the closed-loop system  
150x113mm (600 x 600 DPI)